Lensless Imaging of Red Blood Cells Using Coherent Soft X-ray Scattering

by

Arvin Nazerzadeh-Yazdi

B.Sc., Simon Fraser University, 2004

A THESIS SUBMITTED IN PARTIAL FULFILMENT OF
THE REQUIREMENTS FOR THE DEGREE OF

Master of Science

in

The Faculty of Graduate Studies

(Physics)

THE UNIVERSITY OF BRITISH COLUMBIA

March, 2007

Abstract

I am reporting on lensless imaging of human red blood cell using coherent x-ray scattering (CXS) technique. The successful microfabrication of a sample-mask structure using focused ion beam (FIB) milling was the key element in this imaging technique. The sample-mask structure is 600 - 800 nm gold films deposited using sputtering or electron beam evaporation on Si_3N_4 membrane windows. We used commercially available 100 nm thick Si_3N_4 membranes held by 3 mm diameter silicon frames that are designed for use in transmission electron microscopy. The red blood cell (RBC) sample was mounted in front of a 3 μm hole milled through both gold and Si_3N_4 layers on the opposite side. Three smaller reference apertures with diameters 300, 250 and 200 nm on the gold side were milled all the way through both layers at a distance of 9 μm center-to center from the sample aperture. These holes are used for holographic lensless x-ray imaging. It was found that a gold surface roughens during ion milling due to a sputter instability and which produces cup-like features with a characteristic length up to few hundred nm. We found apertures milled through gold films deposited by sputtering show good circularity and sidewall roughness of 20 nm.

We present result on CXS measurements in transmission geometry near Fe L_3- and C K-absorption edges on a single RBC. We captured high resolution images of the sample by simple Fourier inversion of the recorded far-field scattered intensity. We found 8.5 % reduction in the transmission intensity near Fe L_3-edge due to presence of Fe in the form of hemoglobin molecules inside RBC. This absorption agrees with estimated agrees well with the estimated value of 9 % within experimental uncertainty. From limited data measured below C K-edge we measured a presence of at least 300 nm thick carbon inside RBC which lies in the range of the estimated value of 1.8 μm. The resolution of our lensless imaging technique is about 55 nm near Fe L_3-edge and 78 nm near C K-edge.

Table of Contents

List of Tables

List of Figures

Acknowledgments

I wish to express my deepest appreciation to my supervisor, Dr. Tom Tiedje, for his sincere guidance, encouragement and patience throughout the entire period of this project. His enormous experimental experience and theoretical insight have been invaluable to this work. I consider myself very lucky to have had an advisor who always had time to discuss physics, and was tolerant of my ignorance.

This multidisciplinary project required contribution from long list of people. I will mention a few in order to keep the tradition of gratitude alive. I would like to thank Dr. George Sawatzky for his invaluable discussion throughout the project and comments upon reading this thesis. I am very grateful to Dr. Stefan Eisebitt, Dr. Kyle Shen, Dr. Jochen Geck, Dr. Alexei Nefedov and Stefan Bushhorn for helping with the x-ray measurements at BESSY. Many thanks to Bill Schlotter at Stanford, for many useful discussion on FIB fabrication and x-ray coherent scattering experiments. I was truly overwhelmed by his hospitality just a few days before BESSY measurements at Stanford, his tour of SSRL coherent x-ray scattering beamline was very informing. I wish him the very best life has to offer him. I acknowledge members of Evan Evans group at UBC hospital, Andrew Leung and Dr. Benjamin Smith in helping through preparing the red blood cells and using their setup at UBC hospital. We shared many hours of frustration over mounting the cells on the susbatrates. I would like to thank Dr. Karen Kavanagh and Dr. Li Yang at SFU for assisting and training me on the FIB system over there. I would also like to thank members of MBE lab for numerous assistant including, Kevin Mitchell (lots of help with Matlab programming and Linux matters), Mike Whitwick (for cleanroom training and outstanding assistance through any matter), Eric Nodwell (Best Mac IT), Dan Beaton (help with Latex and Machine Shop), Scot Webster, Shawn Penson, Raveen Kumaran, Anders Ballestad, Erin Young, Ryan Lewis, Johanna Hansen, Ivan-Cristophe Robin, Nikolaj Zangenberg. Special thanks to Jim MacKenzie, our reserch engineer, for his numerous technical help with e-beam evaporator, SEM and even FIB at SFU.

Nearly last, but not least, I thank my parents Nitra and Ali and my brother Arash for their

understanding and encouragement during the course of my work. I thank you for all your moral support.

Dedication

In loving memory of
Khalil Famili,
my grandfather and my best friend.

Chapter 1

Introduction

In many fields of science in order to have deeper level of understanding about the mechanism involved in atomic and molecular processes demands for ability to visualize components present at the atomic or molecular scale. This is occurring in fields as diverse as whole-cell imaging in biology, the study of minimum energy pathway for crack propagation in brittle solids, and the internal structure of the new labyrinthine mesoporous structures developed by inorganic chemists for a wide range of applications [1].

The field of lensless imaging using coherent x-ray scattering (CXS) is expected to make a significant contribution to this effort. In this method, which has been practiced over a decade [2–4], an image is reconstructed from measurement of the far-field Fraunhofer scattered intensity of an isolated and non-periodic object. The resolution of this form of microscopy is limited only by the wavelength and the largest scattering angle recorded. Hence this method is being pursued as a method for high resolution x-ray microscopy without the technological limitation of manufacturing high resolution optical elements [5–8]. In the experiment one measures the intensity of the scattered wave field rather than recording the phase and amplitude separately, thus the main challenge is to retrieve the lost phase information of the scattered electric fields from intensity measurement.

High-resolution images of biological samples are currently made by at least three methods: (*i*) zone-plate x-ray microscopy [9–12]; (*ii*) transmission electron microscopy [13, 14]; (*iii*) x-ray crystallography. All three have particular strengths and limitations. The water-window [10–12] and multi-keV [15] are currently limited to $\approx$ 20 nm resolution by details of the zone-plate resolution, depth of field, and operation [16]. On the other hand, high resolution transmission electron microscopy, although capable of extraordinary resolution, are limited by multiple electron scattering to specimens thinner than 0.5 - 1 μm [13, 17]. The third method, x-ray crystallography, traditionally yields the highest resolution structures and is the structural technique of choice, but it is limited to specimens that can be crystallized [16].

The method is conceptually simple. The specimen (in our case a single red blood cell) is mounted on a thin sample-mask support film, such that it acts as the sole source of scattering. The peculiar, bioconcave-discoidal, shape of the mammalian red blood cell (RBC) has intrigued many scientists in theoretical physics and clinical medicine ever since its first observation following the invention of sufficiently magnifying microscopes [18]. It has been known more than 50 years [19] that a variety of agents can modify the discoid shape of the RBC systematically and reversibly at constant area and volume. The mechanism behind the changes in the shape have been described in [20] and references therein. Meanwhile developing a microscopic technique which can image, with molecular resolution, the changes in the microstructure of the cells remains a challenge. The RBC consist of a composite membrane (plasma membrane plus membrane skeleton) surrounding a fluid interior which is filled with hemoglobin. Hemoglobin is the protein molecule in red blood cells that carries oxygen from the lungs to the body's tissues and returns carbon dioxide from the tissues to the lungs. The iron contained in hemoglobin is responsible for the red color of blood. The Fe presence inside the cell in the form of hemoglobin can provide opportunity for resonance measurement near Fe L-edges.

In summary, the traditional structural techniques do not provide the capability of imaging an intact RBC with resolution on a molecular scale, and it is toward this end that our present efforts are directed. As a common challenge in the field of microscopy preparing a sample suitable for the specific microscopic technique is the most challenging part. This work presents some new developments toward lensless imaging from biological samples using CXS technique. We present results on x-ray spectro-holography (XSH) from red blood cells near Fe L_3- and C K-edge. The Fe presence inside the cell in the form of hemoglobin provides opportunity for resonance measurement near Fe L-edges. The key element in this microscopic technique is the sample-mask preparation where we follow the recent x-ray spectro-holography experiments performed by Eisebitt *et al.* [21] for lensless imaging of magnetic nanostructures.

Chapter 2

X-ray Sample-Mask Preparation

2.1 Physical Vapor Deposition Processes

Physical vapor deposition (PVD) enables one to deposit almost any type of inorganic materials, metals, alloys, compounds and some organic materials. The PVD processes use has been increasing at a very rapid rate since modern technology demands multiple, and often conflicting, sets of properties from engineering materials, e.g., combinations of two or more of the following: high temperature strength, impact strength, specific optical, electrical or magnetic properties, wear resistance, ability to be fabricated into complex shapes, biocompatibility, cost, etc [22].

The two most commonly used PVD processes are evaporation and sputtering. The deposition rates in each of these processes varies from 1 to 75,000 nm per minute. In general all these PVD processes follow three steps to form deposition[23]:

1. Synthesis of the material to be deposited:
    a. Transition from a condensed phase (solid or liquid) to the vapor phase.
    b. For deposition of compounds, a reaction between the components of the compound, some of which may be introduced into the chamber as a gas or vapor.
2. Transport of the vapors between the source and substrate.
3. Condensation of vapors followed by film nucleation and growth.

In all PVD processes one can independently control each step which gives high flexibility in controlling the structure, properties, and deposition rate of the deposited films. In the following section we focus on deposition of gold films using two conventional PVD processes namely electron beam evaporation and sputter deposition. The deposited film surface morphology is studied using atomic force microscopy (AFM).

2.1.1 Electron Beam Evaporation of Gold

In electron beam evaporator the process of phase transition of the source material to vapor state is carried out using an electron gun. The electron gun simply consists of a cathode and an anode. The electrons are accelerated from the cathode to the anode due to potential difference between the two which lies within the range of few kilovolts up to 20 - 30 kV. In our e-beam system we use a themionic gun which uses resistive heating of a high melting point metal such as tungsten wire as an electron source. The source material is carried inside a water cooled crucible which allows the surface of the source to reach a high temperature without metallurgical reaction between crucible and evaporant.

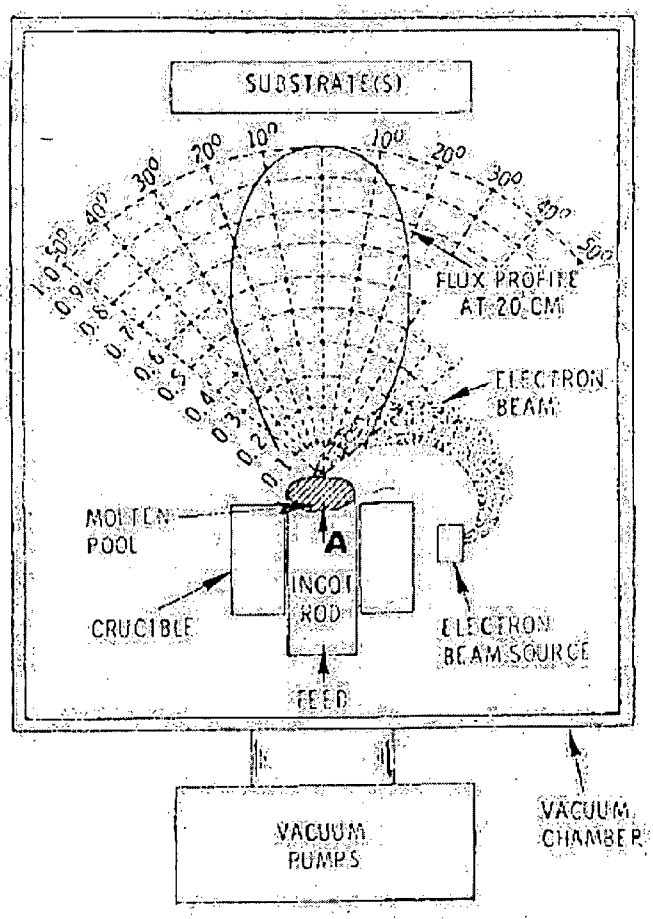

Figure 2.1: Vacuum-evaporation process using electron beam heating. Reprinted from [22].

The e-beam system usually operates under a vacuum range of 10^{-5} to 10^{-7} torr. A schematic of an e-beam evaporation system is shown in Figure 2.1. It can be noticed that the deposition thickness is greatest directly above the center-line of the source and decreases away from it [24]. A uniform thickness ($\pm 10\%$) across the substrate can be obtained by imparting a complex motion to the substrate (e.g., in a planetary or rotating substrate holder) so as to even out the vapor flux on all parts of the substrate; or by introducing a gas at a pressure of 5 to 200 micron into the chamber so that the vapor species undergo multiple collisions during transport from the source to substrate. The latter technique is called gas-scattering evaporation or pressure plating [25, 26].

Characterizing deposition from the e-beam processes involves thermodynamic considerations such as phase transitions from which the equilibrium vapor phase of materials can be derived, as well as the kinetic aspects of nucleation and growth. An excellent treatment of the thermodynamic and kinetic aspect of evaporation processes is given by Maissel [27]. The rate of evaporation is given by the well-known Hertz-Knudsen equation:

$$\frac{dN_e}{A_e dt} = \alpha_\nu (2\pi mkT)^{-1/2}(\overline{p} - p), \tag{2.1}$$

where α_ν is the evaporation coefficient, $dN_e/A_e dt$ is the number of molecules evaporating from a surface area A_e in time dt, $\overline{p}$ is the equilibrium vapor pressure at the evaporant surface, p is the hydrostatic pressure acting on the surface, m is the molecular weight, k is the Boltzmann's constant, and T is the absolute temperature. In addition to vapor flux composition distribution which vary over time or position, all e-beam systems exhibit a vapor spatial density distribution which is nonuniform and dependent upon numerous process variables. It has been reported throughout the literature that atoms ejected from an e-beam target take on a distribution described by [22]:

$$I(\theta) = I_0 \frac{\cos^n \theta}{r^2}, \tag{2.2}$$

where $I(\theta)$ is vapor stream density in a direction θ degrees from the normal to the vapor emitting surface, I_0 is the vapor stream density for $\theta = 0$, and $n = 1, 2, 3$ or more depending on the surface geometry of the evaporant. While the vapor stream emerging from a planar surface element takes on a $\cos\theta$ distribution (where $n = 1$) [27], numerous authors note that e-beam vapor streams rarely exhibit this simple cosine vapor distribution for various reasons described in Figure 2.2 [27, 28], e-beam vapor stream distribution also depend upon the e-beam scanning cycle employed (rate and pattern) and the specific material evaporated [28].

The substrates used for gold deposition are 100 nm thick silicon nitride membranes which are held by 3 mm diameter silicon frames which are commercially available for transmission electron

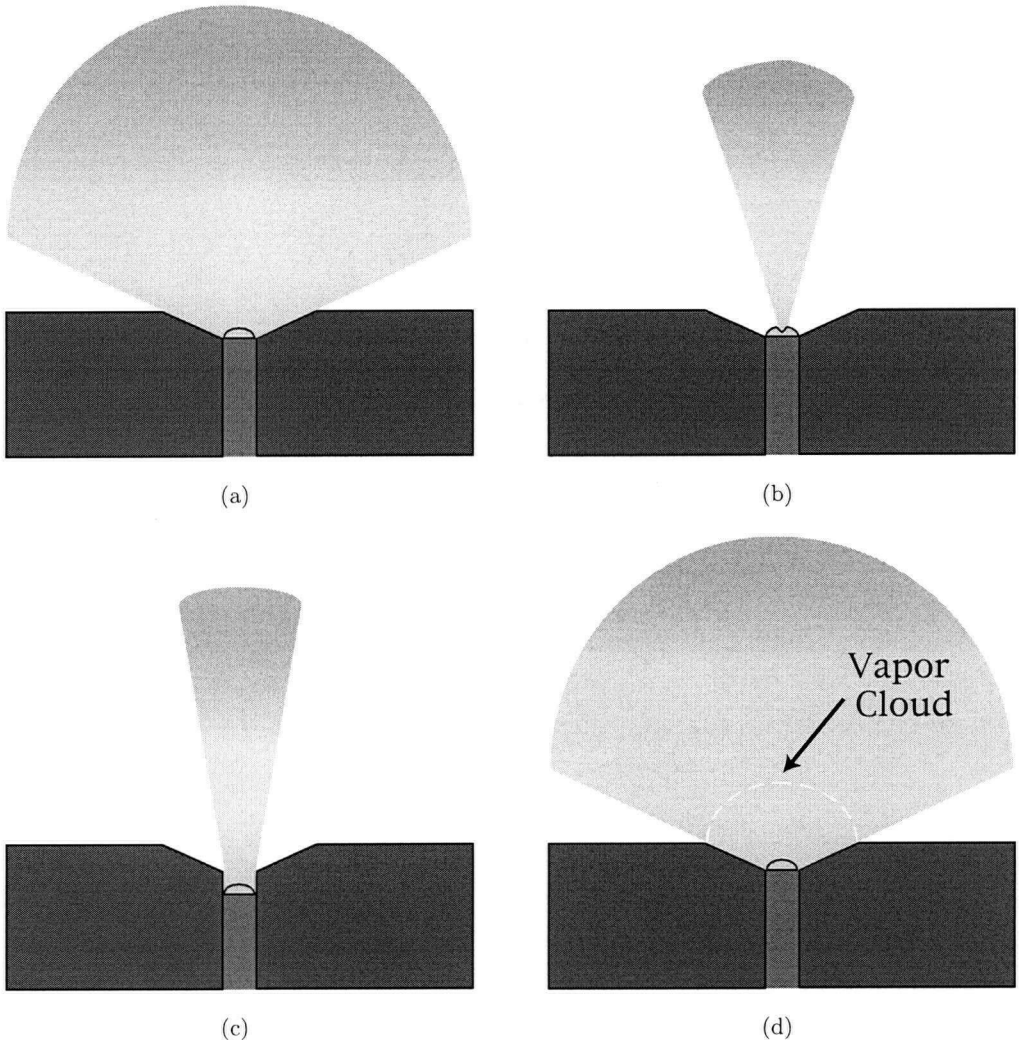

Figure 2.2: E-Beam evaporator vapor flux ditribution. Several factors can combine to modify an e-beam evaporator's vapor flux distribution (a) Formation of a convex vapor emitting surface due to the surface tension of the evaporant; (b) Formation of a concave vapor emitting surface due to local increase in vapor pressure. (c) Obstruction of vapor propagation by the crucible wall due to inadequate feeding of the crucible. (d) Formation of a vapor cloud which, instead of the vapor emitting surface, acts as a virtual source of the vapor stream [28].

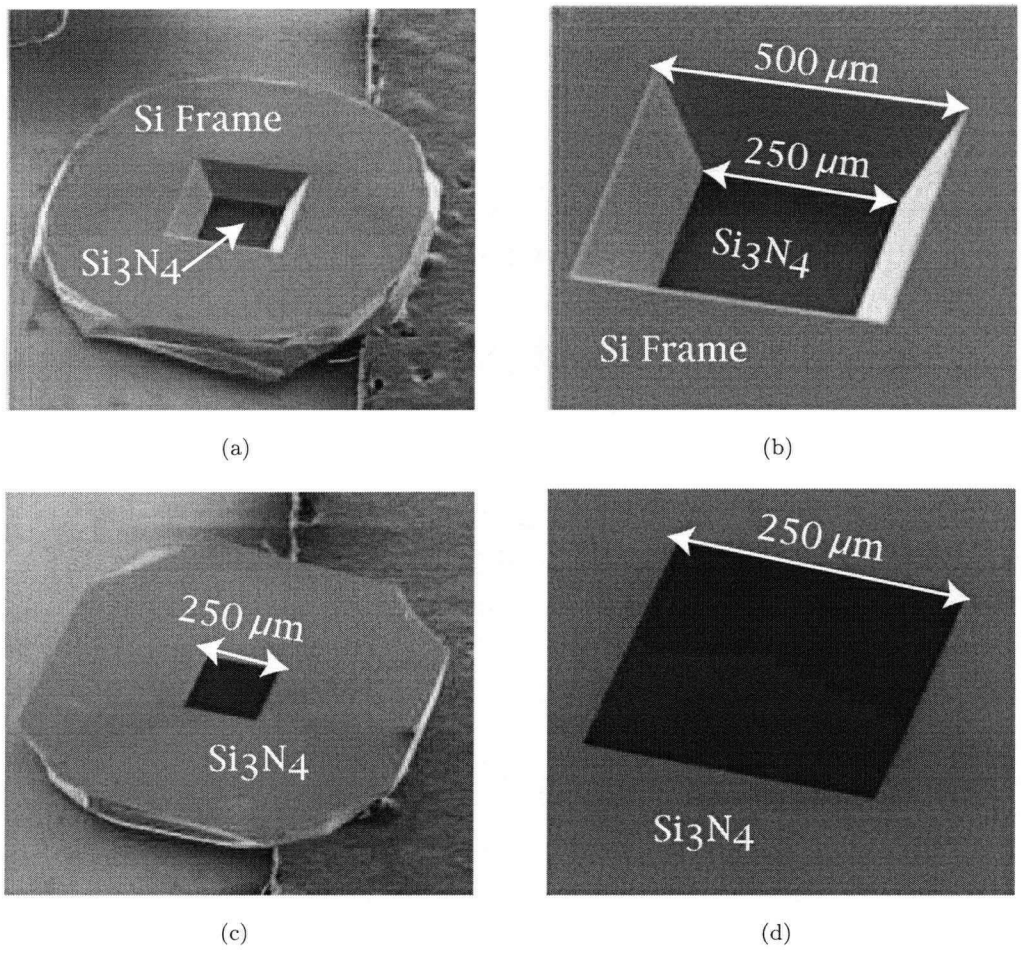

(a) (b)

(c) (d)

Figure 2.3: SEM images of the silicon nitride membrane with windows thickness of 100 nm Si_3N_4 with surrounding silicon support of thickness 200 μm; (a) and (b) shows the front-side, (c) and (d) shows the backside (nitride-side). Total dimensions diagonally in (a) and (c) is 3.0 mm.

microscopy. Scanning electron micrscope (SEM) images of the substrates are shown in Figure 2.3. The substrates were clamped onto a copper block which was tightly attached to a resistive heater and a cold liquid nitrogen line. The temperature is monitored using a K-type thermocouple which was in contact with the heating-cooling stage. The copper block was placed approximately 25 cm vertically above a graphite crucible containing gold material for evaporation. A quartz crystal monitor was positioned close to the substrate for measurement of the thickness of the deposited film. The chamber vacuum is kept in 10^{-6} to 10^{-7} torr range using a cryogenic and a rotary pump.

The substrates were cleaned using an ultra-violet ozone cleaning system for thirty minutes prior to the evaporation. This process removes organic surface contamination and modifies the surface for better adhesion by implanting oxygen on the surface. A thin layer of chromium a few nanometers thick is evaporated at room temperature prior to the gold evaporation. Due to weak surface adhesivity of the gold to the substrate a few nanometers of chromium is used as an adhesive layer prior to the gold deposition. The chromium forms a strong covalent bond with oxide present on the surface of the substrate and metallic bonding between gold and chromium is stronger than gold to an oxidized surface. Gold films of thickness varying from 400 - 800 nm are deposited after the substrates reached the desired temperature. The growth rate was kept within the range of 0.6 - 0.8 Å/s. The deposition of gold using an electron beam evaporator is done for substrates at temperature in the ranges from -100 to 200 °C.

The surface roughness of the Au films deposited on silicon nitride has been studied using atomic force microscope (AFM). The result for e-beam evaporation of 600 nm thick Au films at three different substrate temperatures is presented in Figure 2.4. The gold films deposited at substrate temperature, $T_s \leq 25$ °C present a rolling-hill morphology while a higher temperature affect its surface roughness, with a rough hill-like surface with larger flat top. Two typical length scales are present in the surface morphology $h(\mathbf{x})$, which are the structure height and the lateral structure size (i.e. grain diameter). As quantitative measures, the root mean square (RMS) roughness,

$$RMS = \sqrt{\langle h(\mathbf{x})^2 \rangle_{\mathbf{x}}}, \tag{2.3}$$

and the average grain diameter estimated by $L_c = 2\pi/q_c$, where q_c is the spatial frequency corresponding to the highest power in the radially averaged power spectral density $C(q)$,

$$C(q) = \langle |\mathcal{F}[h(\mathbf{x})]|^2 \rangle_{|\mathbf{q}|=q}. \tag{2.4}$$

The log-log scale plot of $C(q)$ for Au films deposited at different temperature is shown in the

Figure 2.5 along with the line of slope $m = -2$. The value of q_c is determined by the point asymptote to the slope -2 line, since it corresponds to the highest power density in the log-log scale radially averaged PSD plot. In terms of the surface parameter the values of L_c found this way agree well with the average grain size in the AFM images. The values of RMS surface roughness and grain diameter L_c for the samples with different substrate temperature, T_s, are tabulated in Table 2.4 . The films deposited below -100 °C ended up peeling off the surface due to thermal expansion mismatch between the substrate and the gold films. We found that RMS roughness and grain diameter increases through increasing T_s which compares with the results by Golan [29] and Semaltianos [30]. In principle the surface roughness is determined by the statistical process of nucleation and growth and the surface mobility of adatoms. At low deposition temperatures the mobility of the adatoms is small which leads to formation of smaller grain sizes with a sharper peak. At higher deposition temperatures the surface mobility of adatoms increases and the condensation can occur preferentially at the surface concavities and this tends to smooth the surface of the film. There is evidence of epitaxial growth of Au films on Mica and glass for $T_s > 400$ °C [30, 31].

Sample	T_s	RMS (nm)	L_c (nm)
SCA009	200°C	16.8	208
SNCRAU7	25°C	4.7	89
SCA007	-100°C	2.2	70

Table 2.1: Root mean square and averaged grain size, L_c, of Au surfaces deposited on Si_3N_4 at different substrate temperature.

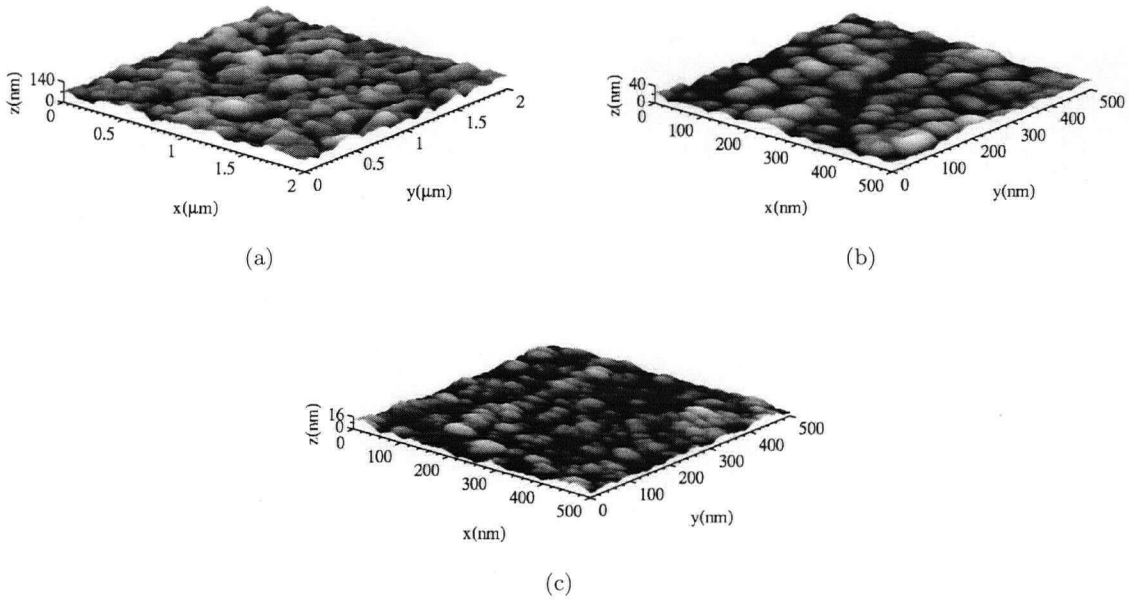

Figure 2.4: AFM images of Au surfaces deposited using e-beam evaporator at substrate temperatures (a) T_s = 200 °C; (b) T_s = 25 °C and (c) T_s = -100 °C.

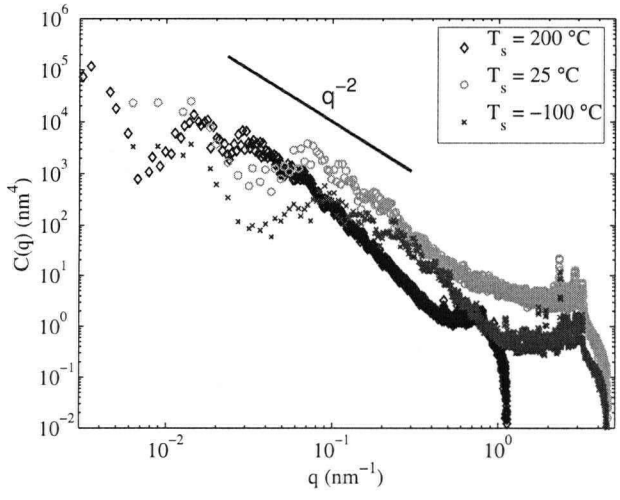

Figure 2.5: Radially averaged power spectral densities $C(q)$ calculated for Au surfaces deposited using e-beam evaporator at substrate temperatures T_s = 200, 25 and -100 °C. From the plot the average grain diameter $L_c = 2\pi/q_c$= 208, 89 and 70 nm respectively.

2.1.2 Sputter Deposition of Gold

In the sputtering process gas ions from a plasma are accelerated towards a target consisting of the material to be deposited. Material is detached (sputtered) from the target and afterwards deposited on a substrate in the vicinity. The process is realized in a closed vacuum chamber, which is pumped down to a vacuum base pressure before deposition starts (see Figure 2.6). To enable the ignition of a plasma usually argon is fed into the chamber up to a pressure between 1 - 3 mtorr. By natural cosmic radiation there are always some ionized Ar^+ ions available. In the dc-sputtering a negative potential U up to some hundred volts is applied to the target. As a result, the Ar ions are accelerated towards the target and set material free, on the other hand they produce secondary electrons. These electrons cause a further ionization of the gas. The number of atoms N per unit area per second leaving the target is given by

$$N = \frac{J_+}{ge} S(V, \mathrm{A}, \mathrm{B}), \tag{2.5}$$

where J_+ is the current density of the bombarding ions, g is the number of electronic charges per ion, and S is the sputter yield in atoms per incident ion, which is a function of the ion energy V, the ion species A, and the target material B.

A stable burning plasma is required to have a sufficient amount of ions available for sputtering of the target material. This can be done by increasing the pressure of the sputtering gas which gives rise to a higher degree of ionization. In practice to increase the ionization rate by emitted secondary elecrons even further, a ring magnet is located below the target in magnetron sputtering. The electrons in its field are trapped in cycloids and circulate over the target's surface. By the longer dwell time in the gas they cause a higher ionization probability and hence cause plasma ignition at pressures, which can be up to one hundred times smaller than for conventional sputtering. This can provide higher deposition rates. On the other hand less collisions occur for the sputtered material on the way to the substrate because of the lower pressure and hence the kinetic energy at impact on the substrate is higher. The electron density and hence the number of generated ions is highest, where the B-field is parallel to the substrate surface normal. The highest sputter yield happens on the target area right below this region. An erosion zone is formed which follows the form of the magnetic field.

The bombardment of a non-conducting target with positive ions would lead to charging of the surface and subsequently to a shielding of the electrical field. The ion current would die off. Therefore the dc-sputtering is restricted to conducting materials like metals or doped semiconductors. There are two ways to produce dielectric films: in rf-sputtering (radio frequency)

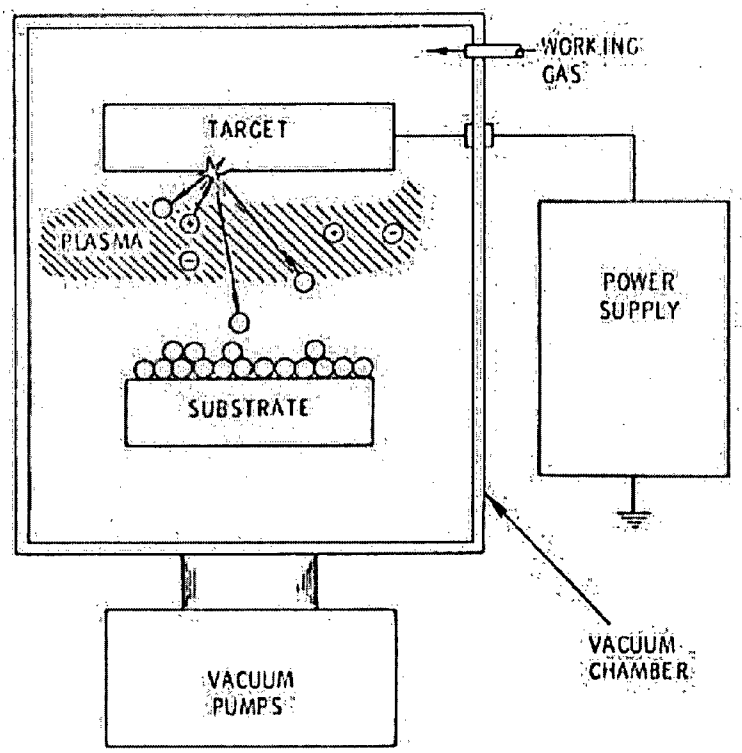

Figure 2.6: Schematic diagram showing basic sputtering process. Reprinted from [22].

an ac-voltage is applied to the target. In one phase ions are accelerated towards the target surface and sputter material. In the other phase charge neutrality is achieved. Sputtering of non-conducting materials is possible with RF. Alternatively, for reactive sputtering other gases like oxygen or nitrogen are fed into the sputter chamber in addition to argon, to produce oxidized or nitrided films.

Gold films are deposited on the silicon nitride substrates described in the last section using Anatech Hummer 6.2 DC magnetron sputtering system at Simon Fraser University. This system uses 3000 volts and 30 mA DC power supply and allows deposition cycles no longer than 15 minutes. The substrates were cleaned with ozone and mounted on the scanning electron microscope (SEM) stubs. Before starting the plasma the chamber is purged with Ar three times to minimize any residual gases inside the chamber. The deposition rate was about 0.8 Å/s, whilst the chamber pressure was kept at 60 mtorr and the plasma current was approximately 15 mA. The substrate temperature fluctuation during deposition was kept well below 5 degrees

near room temperature. Film thickness was measured post-deposition with a Tencor Instruments Alpha-step 100 profilometer and was about 600 nm.

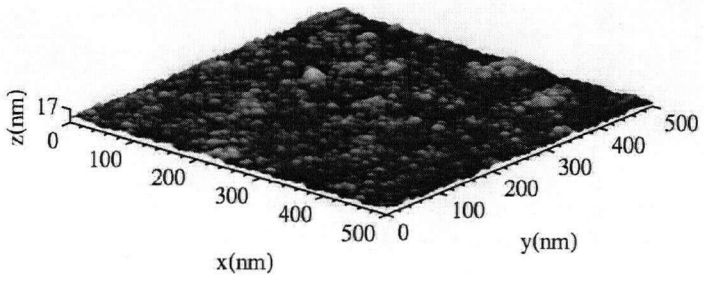

(a)

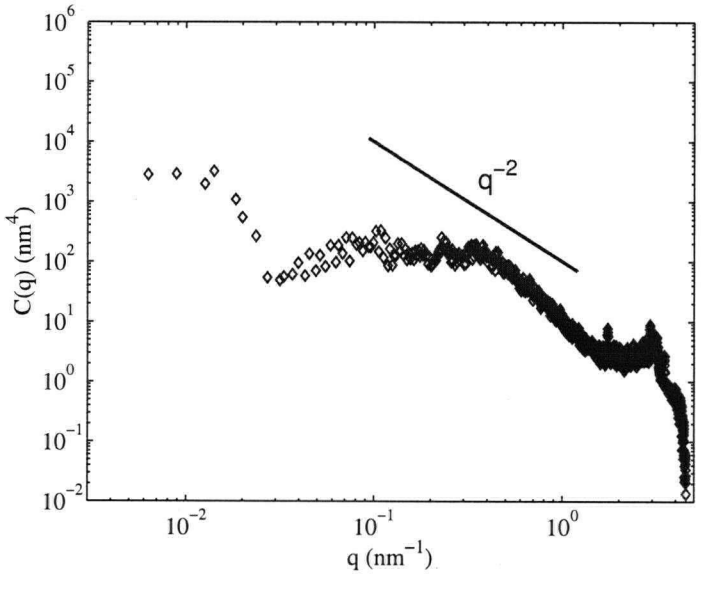

(b)

Figure 2.7: (a) AFM image of 600 nm gold film deposited using sputtering. The RMS surface roughness is about 1.8 nm; (b) radially averaged PSD calculated from the AFM image in (a); the average grain diameter is $L_c = 17$ nm.

The surface roughness of the Au films sputter deposited on silicon nitride membranes was measured using the AFM. The result for sputter deposition of 600 nm thick Au film is presented in Figure 2.7(a). The RMS roughness for this sample was measured to be 1.8 nm. The log-log scale plot of radially averaged PSD of the AFM image in Figure 2.7(a) is presented in Figure 2.7(b).

Repeating the same calculation from the last section we found the average grain diameter L_c = 17 nm.

2.1.3 E-Beam Evaporation versus Sputter Deposition of Gold

The summary of the surface roughness analysis of Au films deposited using sputtering and e-beam evaporation is presented in Figure 2.8. The AFM result showed comparable RMS surface roughness for sputtering and e-beam evaporation at substrate temperatures of -100 and 25 °C respectively. The advantage of sputtering is better adherence of the gold layer along with a smaller grain diameter. The difference in thermal expansion of the substrate and gold films at low temperatures (below -100°C) led to weak adhesion of the gold to the substrate causing the film to peel off the substrate. On the other hand sputtering is an inefficient way to induce a solid-to-vapor transition. Typical yields (atoms sputtered per incident ion) for a 1 KeV argon ion incident on a gold surface is 2.5 [32] where most of plasma power is wasted in the in the form of heating of the target and sample environment. Thus the phase change energy cost is larger than evaporation. Also the utilization efficiency of the target material in magnetron sources can be as low as 20 -30 % [23], which can be improved partially by relative motion of the target with respect to the magnet [33].

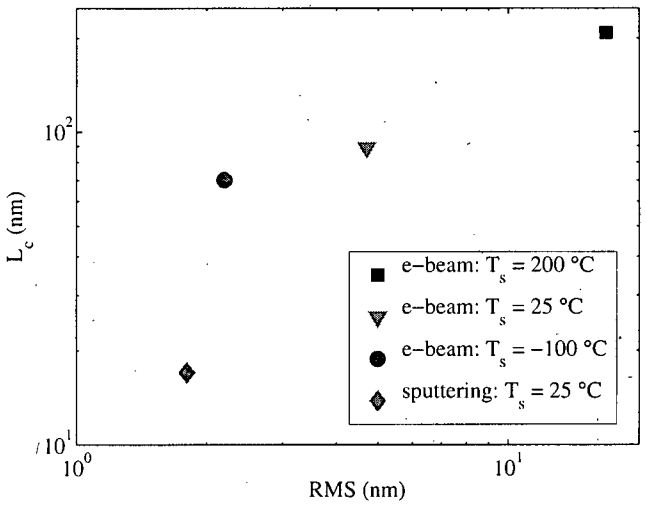

Figure 2.8: Log-log plot of grain size L_c versus RMS roughness of gold films deposited using sputter deposition and e-beam evaporation.

2.2 Microfabrication Using Focused Ion Beam

The basic operating principle of a focused ion beam (FIB) system is shown in Figure 2.9. The system is similar to an SEM, the major difference being the use of a gallium ion (Ga^+) beam instead of an electron beam. The ion beam is generated in a liquid-metal ion source (LMIS). The application of a strong electric field causes emission of positively charged ions from a liquid gallium cone, which is formed on the tip of a tungsten rod. As illustrated in the figure, modern FIB systems involve the transmission of a parallel beam between two lenses. A set of apertures is used to select the beam current and hence the beam size and image resolution. The beam energy is typically 30 keV with a beam current in the range of 1 to 20 nA, and the best image resolution that can be obtained is approximately 5 - 7 nm.

The beam is raster-scanned over the sample, which is mounted in a vacuum chamber at pressures of around 10^{-5} mtorr. When the beam strikes the sample, secondary electrons and secondary ions are emitted from its surface. The electron or ion intensity is monitored and used to generate an image of the surface. Secondary electrons are generated in much greater quantities than ions and provide images of better quality and resolution; consequently the secondary electron mode is used for most imaging applications.

The focused ion beam has been a valuable tool in the semiconductor industry for various applications, including mask repairing, device modification, failure analysis, and integrated circuit debugging [34]. Because of the very short wavelength and very large energy density, the FIB has the ability for direct fabrication of structures that have feature sizes at or below one micrometer which makes it one of most popular tools in fabrication of microdevices and high-precision components. In the following we describe the FIB flux characteristics and its application in patterning circular apertures in the gold films prepared in the last section.

2.2.1 Focused Ion Beam Flux Characteristic

In the modern computer-controlled FIB machine, milling of any patterns involves precise pixel-by-pixel movement of the ion beam. A simple example is milling a microchannel. This is done by moving the ion beam across a series of adjacent pixels representing the path of the microchannel as shown in Figure 2.10. The amount of time the beam remains on over a single pixel is called the dwell time, t_d, and the pixel spacing is labeled by, p_s. To mill a channel with uniform cross sections, the ion flux with respect to the scan direction has to be constant. To achieve this, the

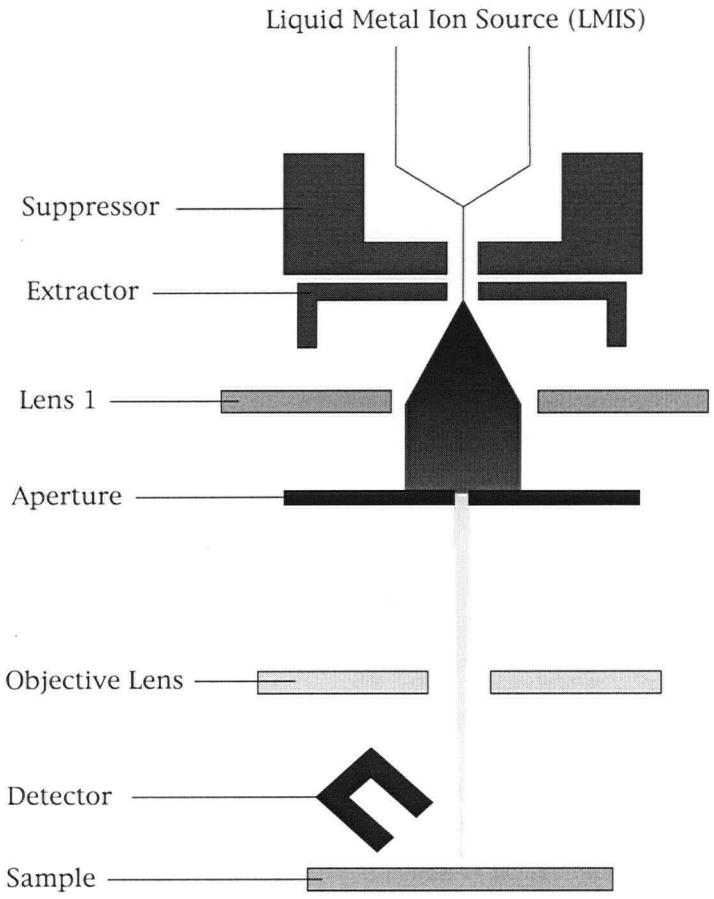

Figure 2.9: Schematic diagram of an FIB system describing basic principle in focused ion beam operation.

pixel spacing must be small enough to allow a proper overlap between adjacent pixels so that a smooth channel with a constant cross section is obtained. As a result, the threshold value for the minimum amount of beam overlap is very important.

The flux distribution of the FIB is described by a Gaussian distribution as proven by many authors [35–37], which mathematically can be represented as

$$D(r,\sigma) = \frac{D_0}{\sigma\sqrt{2\pi}} \exp\left[-\left(\frac{r-r_0}{\sigma\sqrt{2}}\right)^2\right], \tag{2.6}$$

where D is the Gaussian distribution; D_0 is the ion dose constant; r is the radial coordinate; the beam center is located at $r = r_0$ and σ is the standard deviation of the Gaussian distribution, in which the beam full width at half maximum (FWHM) diameter, d_f, is equal to 2.355σ. Commonly the FWHM is used for defining the beam diameter. The total number of ions impinging

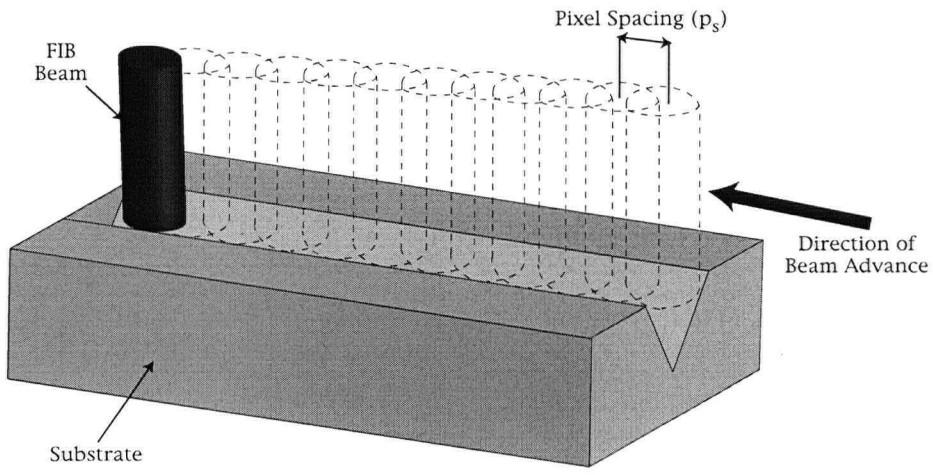

Figure 2.10: Schematic diagram describing milling of a microchannel.

on the target within one dwell time (t_d), is $I_p t_d/(nq_e)$, where I_p is the beam current and n is the number of charge, in which $n = 1$ is for single-charged Ga^+ ion beams. Here q_e is the charge of one electron which is equal to 1.6×10^{-19} C. Thus, the total beam input energy becomes $E_e I_p t_d/(nq_e)$, where E_e is the energy of one ion. Then, the constant D_0 can be obtained by satisfying the conservation of energy in which the total input dose equals the total kinetic energy of the ions to the target within one dwell time, i.e.,

$$\int_0^{2\pi}\int_0^{\infty} D(r,\sigma) r dr d\theta = \frac{E_e I_p t_d}{nq_e}. \tag{2.7}$$

Substituting Eq. (2.6) into the above equation, one can have

$$D_0 = \frac{E_e I_p t_d}{nq_e \sigma\sqrt{2\pi}} = 0.94\frac{E_e I_p t_d}{nq_e d_f}. \tag{2.8}$$

If $D(r,\sigma)$ represents the ion beam input energy density, D_0 can be found as

$$D_0 = 0.94\frac{I_p t_d}{nq_e d_f} \tag{2.9}$$

The energy of the ions are measured in electron volts (eV). For example for 30 keV Ga^+ FIB, single-charged ions need to be accelerated through a differential potential of 30 kV. During milling, since the beam moves in a pixel-by-pixel motion and stays at each pixel for a time equal to t_d , the superimposed or overlaid ion intensity (or density) over the target substrate can be conveniently expressed by the Cartesian coordinates (x, y) as

$$D(x,y,\sigma) = \frac{D_0}{\sigma\sqrt{2\pi}} \exp\left[-\left(\frac{y-y_0}{\sigma\sqrt{2}}\right)^2\right] \times \sum_{n=0}^{N} \exp\left[-\left(\frac{x-x_0-np_s}{\sigma\sqrt{2}}\right)^2\right] \tag{2.10}$$

where N is the total number of pixels involved in the process. During milling, the beam center starts at $(x, y) = (x_0, y_0)$ and moves along the x direction. Figure 2.11 shows the normalized ion flux or intensity at different normalized pixel spacing (p_s/σ), where the normalized ion intensity (or density) is defined as $\overline{D} = \sigma\sqrt{2\pi}D/D_0$. The Cartesian coordinates are also normalized by the standard deviation, σ.

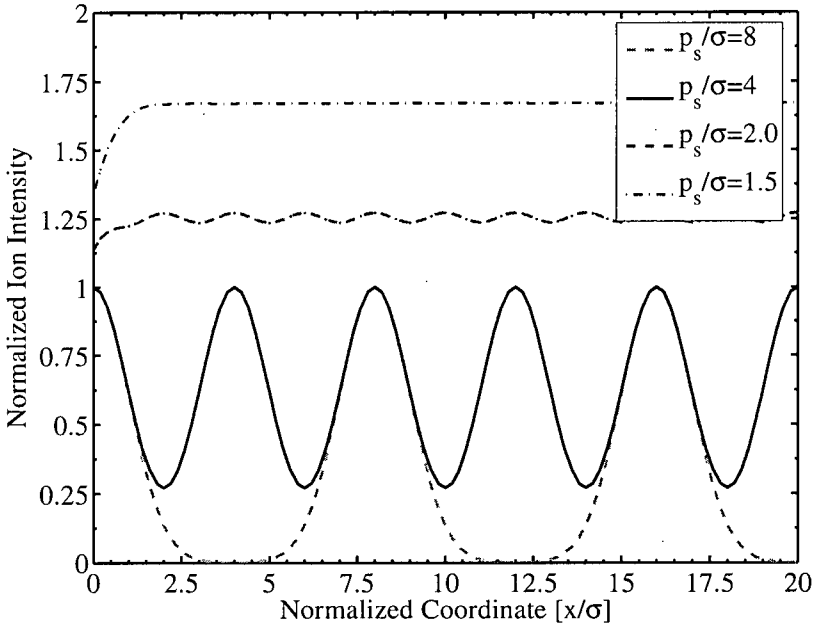

Figure 2.11: Overlap effect on ion intensity distribution for Gaussian FIB milling.

As shown in Figure 2.11, at $p_s/\sigma = 8$, the ion flux of milling resembles each individual Gaussian distribution and no measurable overlap is observed, while a small portion of overlap is observed at the tail regions when $p_s/\sigma = 4$. As p_s/σ decreases to 2, the fluctuation of the ion flux becomes less than 3 % of its mean. Finally, the fluctuation disappears as p_s/σ reaches 1.5 and the normalized ion flux becomes stable and converges to a constant of 1.671, i.e., the fluctuation becomes immeasurable, less than 0.01%. The condition of $p_s/\sigma = 1.5$ is equivalent to $p_s/d_f = 0.637$ for a Gaussian distributed beam. To clearly illustrate the ion flux distribution, the 3D profiles for p_s/σ equal to 1.5 and 3.0 are shown in Figure 2.12. This clearly indicates that to have a uniform scanning ion flux in channel milling, the normalized pixel spacing should be equal to or smaller than 1.5 (or $p_s/d_f = 0.637$), while a drilling process for making an array

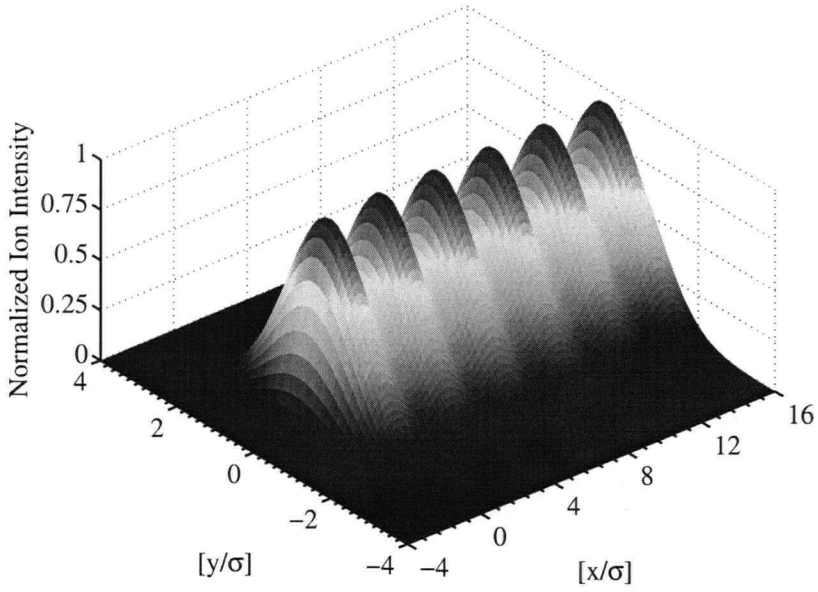

(a)

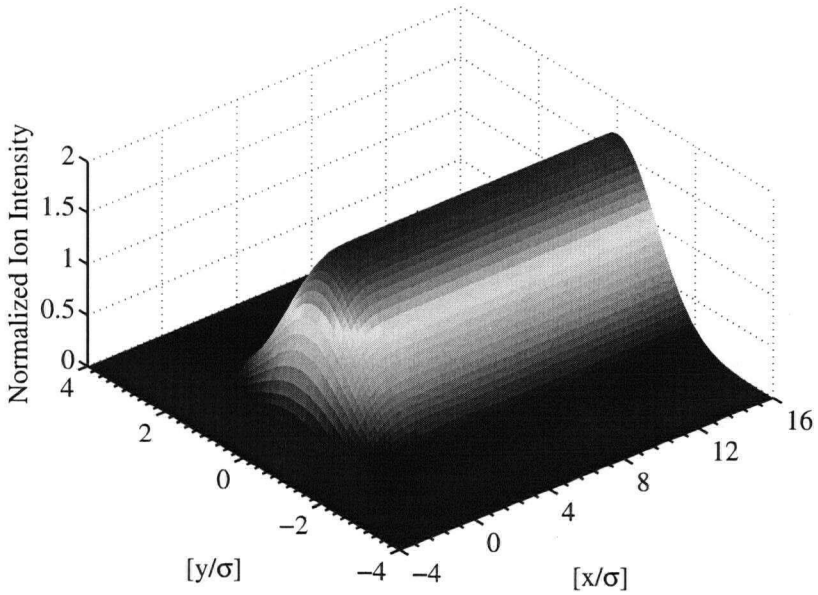

(b)

Figure 2.12: Three-dimensional normalized ion intensity distribution in FIB milling; (a) normalized pixel spacing equal to 3.0; (b) normalized pixel spacing equal to 1.5.

of holes would require the normalized pixel spacing to be larger than 7 or 8. As a result, the drilling process can be considered as a special case of channel milling.

2.2.2 FIB Milling Circular Apertures through Gold Films

The gold films deposited as described in sections 2.1.1 and 2.1.2 were patterned using a dual-beam FIB system (FEI Strata 235) at Simon Fraser University. This FIB system operates with a 30 KeV Ga^+ ion beam with the total beam current up to 20 nA. The beam current can be reduced to 1 pA using a beam defining aperture. The relation between the beam current and the beam spotsize on the sample is shown in Table 2.2. In the current experiment we used mostly 30 and 10 pA beam current for the milling. The samples were mounted on SEM stubs with Au films facing the beam. In this dual-beam system the ion column and electron column are positioned at 52 degree with respect to each other. The optimum sample position for ion milling is shown in Figure 2.13, where the sample is facing the ion beam perpendicularly with the plane normal at 52 degree with respect to the electron column at a distance of 5 mm.

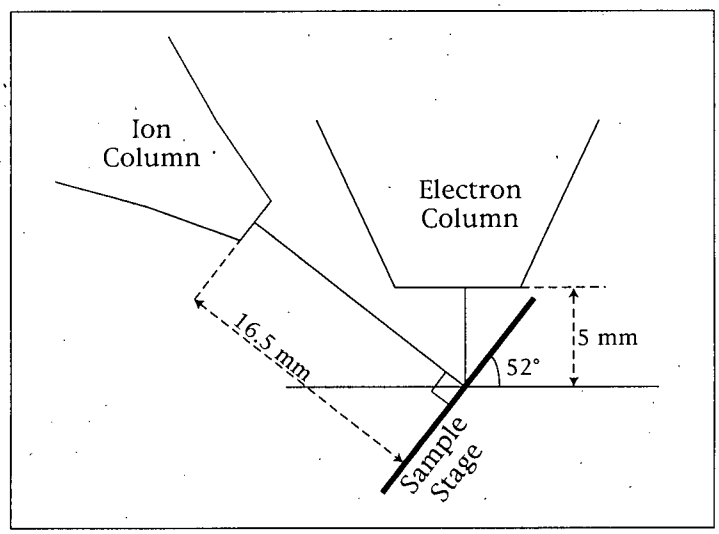

Figure 2.13: Schematic of focused ion beam dual-beam geometry.

The circular pattern is drilled using the pre-defined circle pattern function on the xP dual-beam software. This pattern is fabricated by rastering along a spiral path to cover the whole circular pattern (see Figure 2.14). The dwell time is set to 1.0 μs with an overlap of 50% between each pixel point. This automatically satisfies the condition $p_s/d_f < 0.639$. The data

Beam Current (pA)	Lens 1 Voltage (kV)	Milling Spotsize (nm)
1	1.0	6
10	14.5	10
30	16.0	12.5
50	17.5	15
100	21.5	20
300	24.5	25
500	25.0	30
1000	25.5	35
3000	27.5	60
5000	28.3	100
7000	28.5	150

Table 2.2: Focused ion beam full-width half maximum for different beam current.

acquisition board (DAQ) which is responsible for linking the FIB system to the computer has 12-bit resolution, thus each image contains $2^{12} \times 2^{12}$, or (4096×4096) pixels which are accessible directly for programming any possible pattern. There is also a memory restriction on the DAQ board which doesn't allow access to more than a million points at a time. Thus for optimum results one should minimize the pixel spacing and the beam aperture for fine milling; p_s is chosen so that the ratio p_s/d_f is lower than 0.639 and the total number of pixels covering the whole pattern stays below 2^{20} pixel points. The pixel spacing is derived by dividing the horizontal field of view (HFW) of the image by 4096 (DAQ conversion resolution). As an example at a magnification of 25,000 the pixel spacing is about 1.5 nm, and using a 10 pA current ($d_f = 10$ nm), thereby $p_s/d_f = 0.15 < 0.639$. The total milling time, t, can be calculated by knowing the sputter yield (Y_D) of the material to be milled from the relation:

$$t = \frac{n_a V q_e}{I_p Y_D}, \tag{2.11}$$

where n_a is atomic concentration (atoms/cm^3), V is the total volume of material which is about to be sputtered, I_p is the ion beam current and q_e is the charge of a Ga^+ ion which is 1.6×10^{-19}. This relation neglects any redeposition or refocussing effects during sputtering. For Au the sputter yield, Y_D, for a 30 keV Ga^+ ion, with ion beam current of 10 pA, is estimated to be 15 atoms/ion [34], which yield a total milling time about 355 seconds for a circular holes with

diameter 3 μm and depth of 800 nm. In practice we found milling continuously over this period of time leads to a larger redeposition and sputtering at the edges of the hole compared to breaking the whole milling period into multiple steps. This will minimize any surface artifacts introduced by the beam instability however the trade off is the overall process time is more than twice as long.

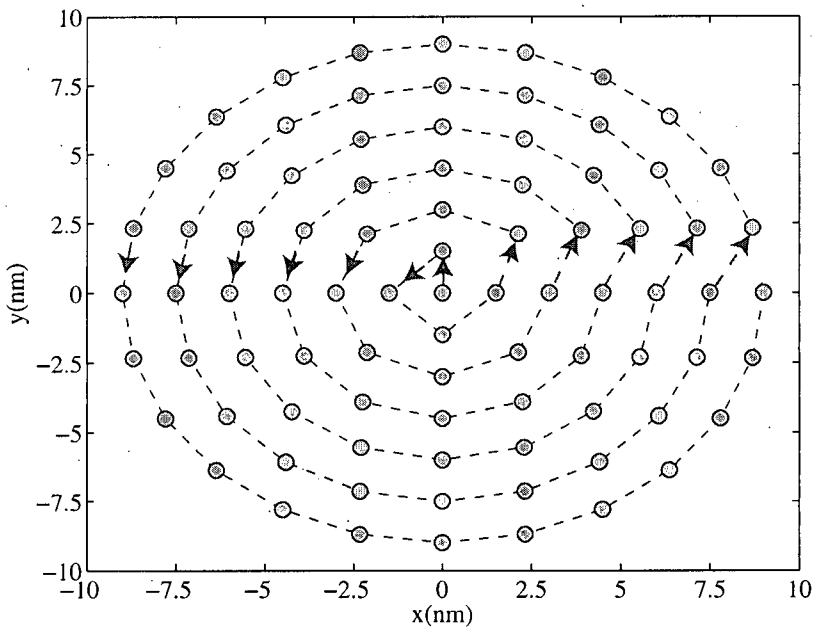

Figure 2.14: Circular milling pattern used by FIB system for milling circular pattern. The dwell time is constant over the whole sets of pixels.

For best x-ray imaging results, the focused ion beam milling should produce a circular aperture in the gold film with smooth vertical sidewalls, exposing the Si_3N_4 membrane at the bottom with no punctures, surface roughness or residual gold. SEM images of 5 μm diameter holes milled through 400 nm gold for different milling depth along with the AFM images of the surface roughness of the bottom of the holes are shown in Figures 2.15 and 2.16. We find that the gold surface roughens during ion milling due to a sputter instability [38] producing cup-like surface features (known as sputter ripples) with a characteristic length up to a few hundred nm. These features are imprinted on the membrane during the milling and cause pinholes to form in the membrane before the gold is completely removed from the bottom of the aperture. Since the gold has a considerably higher sputter yield than silicon nitride, as ion milling reaches the silicon

nitride layer the roughness starts to relax to a lower value. The summary of surface roughening through milling time is presented in Figure 2.17.

For a constant energy Ga^+ ion beam the surface roughness of the deposited gold along with the depth of the milling are the determining factors in the size of the sputter ripples. Thus artifacts introduced in the nitride layer by the sputter instability can be mitigated by minimizing the roughness of the deposited gold films. The surface roughness of the gold can be reduced by depositing the gold by sputtering rather than electron beam evaporation and by depositing the films on cold substrates (-100°C). Figure 2.18 shows 5 μm holes milled through different gold surfaces along with AFM images of the surface before ion milling. One can see that punctures through the membrane and residual gold spots are minimized for low initial surface roughness. Overall the milled apertures show good circularity and sidewall roughness of 20 nm.

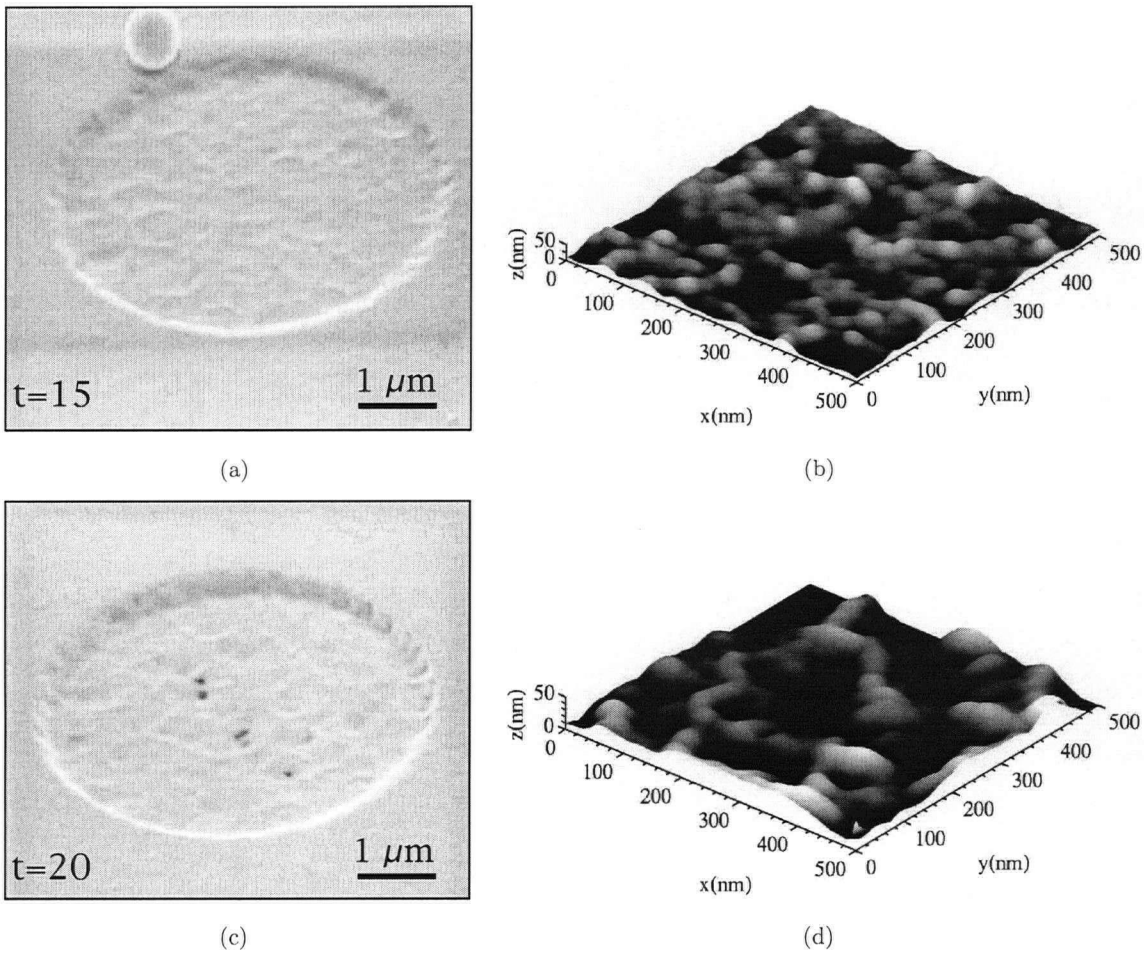

Figure 2.15: The AFM and SEM images of a 5 μm diameter hole milled through 400 nm gold films. t corresponds to the number of times each pixel is exposed to the ion beam for t_d=1.0 μs. The left column shows the SEM images of the apertures, the right column shows the AFM images of the bottom of the hole where the RMS roughness is 6.6 nm and 7.1 nm for (b) and (d) respectively.

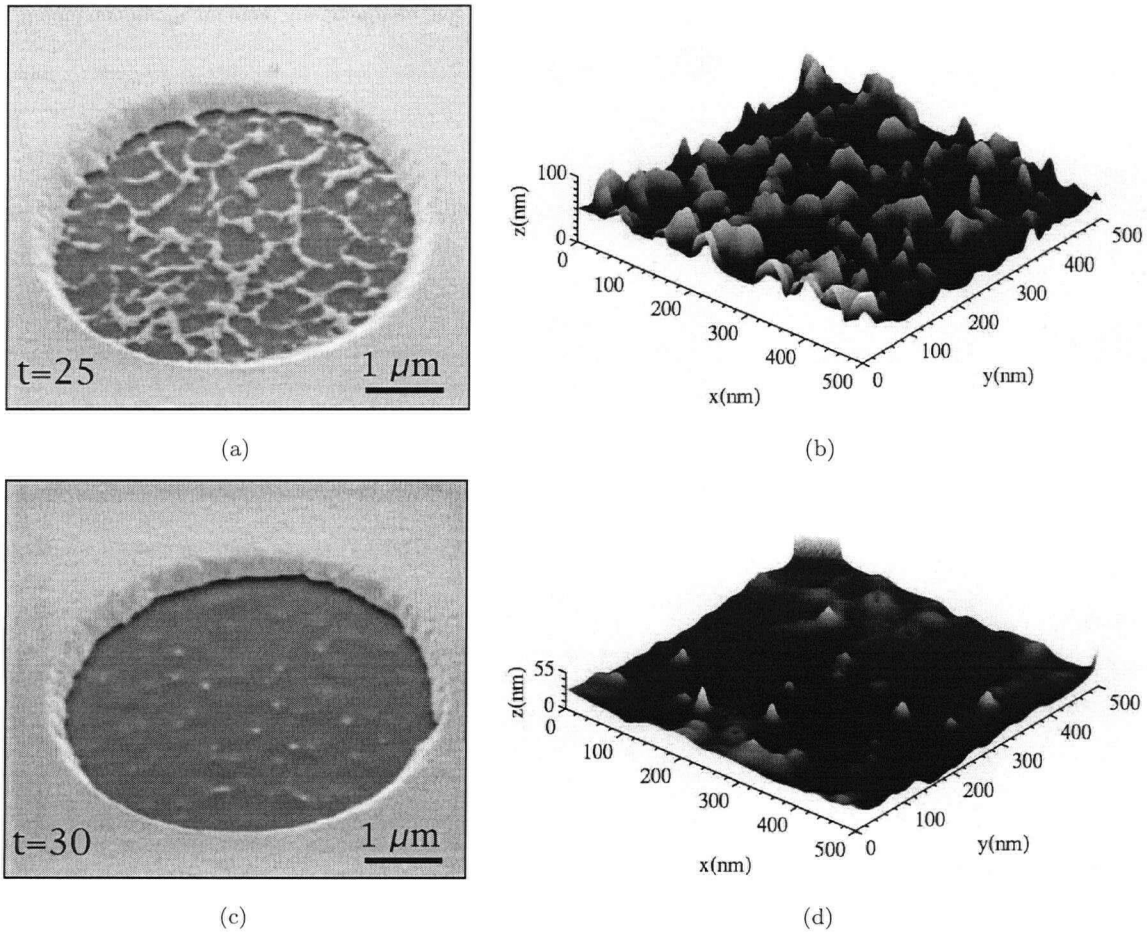

Figure 2.16: The AFM and SEM images of a 5 μm diameter hole milled through 400 nm gold films. t corresponds to the number of times each pixel is exposed to the ion beam for t_d=1.0 μs. The left column shows the SEM images of the apertures, the right column shows the AFM images of the bottom of the hole where the RMS roughness is 13.1 nm and 3.6 nm for (b) and (d) respectively. The nitride layer is reached in (c) which leads to relaxation of the roughness as described above.

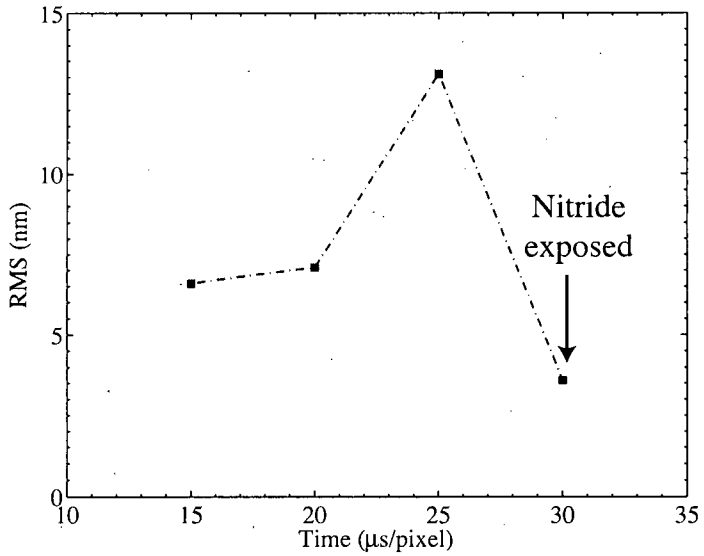

Figure 2.17: The summary of surface roughening through different milling time. The data points are taken from the Figures 2.15 and 2.16. A connected line is for guide to eye.

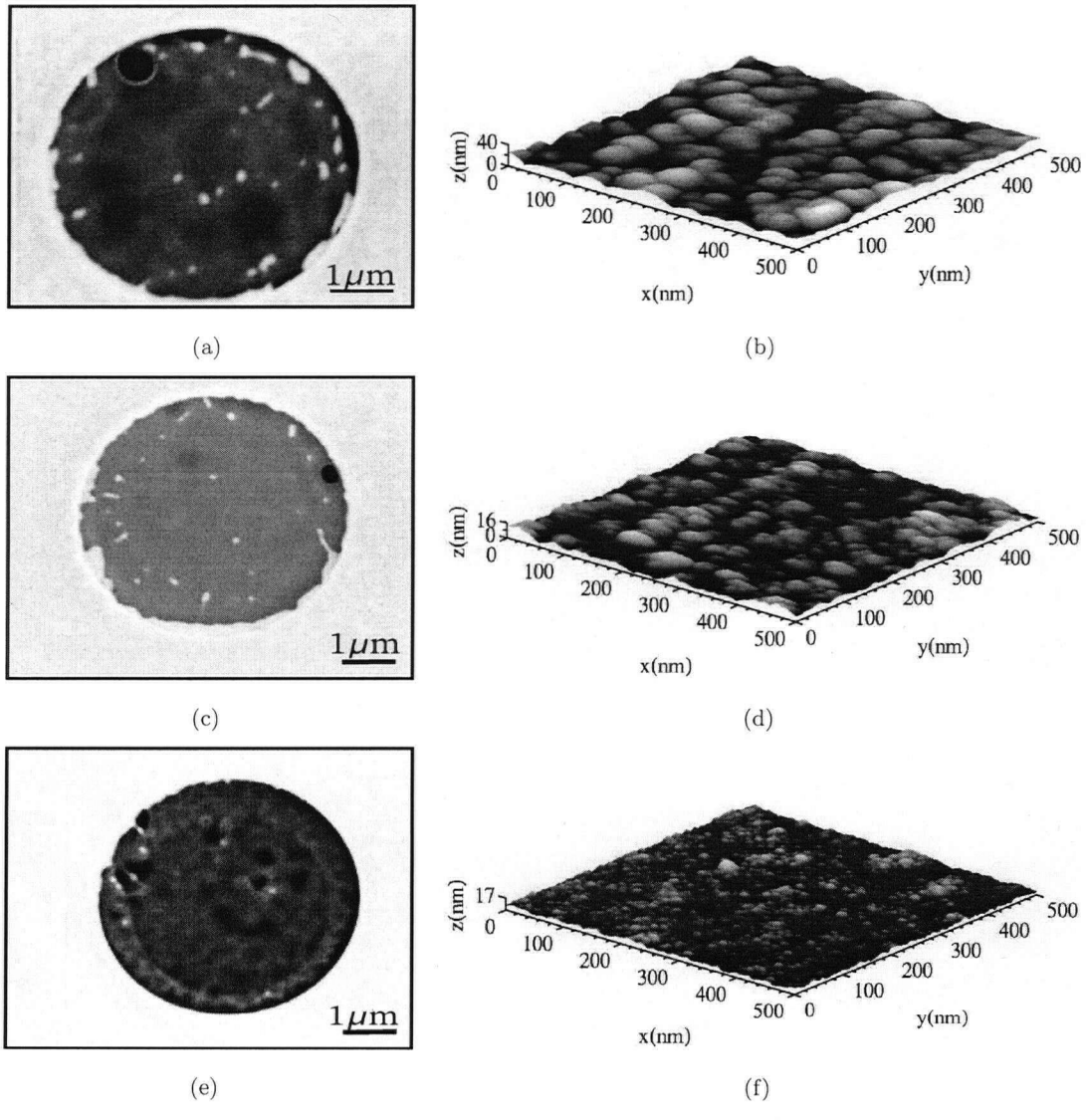

Figure 2.18: SEM (Left Column) images of 5 μm diameter aperture milled through gold films with different roughness due to different deposition processes. AFM (Right Column) images of the Au films before focused ion beam milling. (a-b) e-beam evaporation at T_s = 25°C with RMS roughness = 4.7 nm; (c-d) e-beam evaporation at T_s = -100°C with RMS roughness = 2.2 nm; (e-f) sputter deposition at T_s = 25°C with RMS roughness = 1.8 nm.

2.2.3 X-ray Masks for Lensless X-ray Imaging

The x-ray masks are prepared by FIB milling 3 - 5 μm diameter apertures through gold masks deposited on the silicon nitride membrane windows. In practice for best x-ray imaging results, the FIB milling should produce a circular aperture in the gold films with smooth vertical sidewalls, with relatively smooth silicon nitride at the bottom. As we found in the last section the roughening of the silicon nitride membranes is inevitable due to the sputtering instability. In section 4.1.2 we show x-ray diffraction simulations of different types of apertures illustrating the effect of roughening of the sidewalls and the bottom of the hole, on the diffraction pattern. One solves the problem of roughening of the nitride layer by milling through the nitride layer after drilling through the gold. This however introduces lateral dimension restriction on the actual samples mounted on the mask for x-ray imaging. As long as one of the lateral dimensions of the actual samples is larger than diameter of the objective aperture, it can be securely mounted in front of the object hole. An SEM image of a x-ray sample-mask prepared with FIB milling is shown in Figure 2.19. This sample is milled with 10 pA ion current aperture, with t_d=1.0 μs. The smaller holes drilled through both gold and silicon nitride at a distance of 9 μm from the objective apertures are used for the holographic imaging [21]. The reference apertures have conical shape with diameter of 300, 250 and 200 nm at the (Au) front side and 100, 75 and 50 nm at the (nitride) backside. The tapered shapes comes from the high-aspect-ratio milling. Samples for x-ray imaging are typically mounted on the nitride side in front of the objective aperture without covering the reference holes. In the next chapter we will show how the red blood cells can be prepared to be mounted on these sample masks.

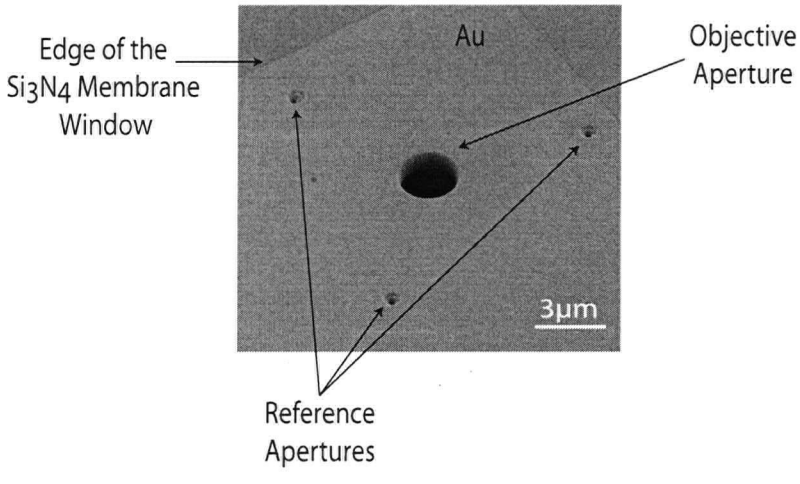

(a)

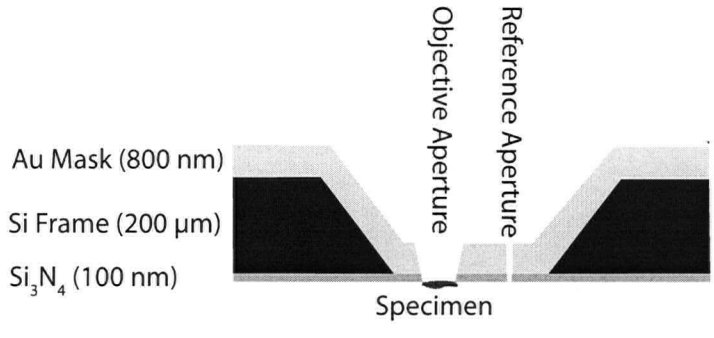

(b)

Figure 2.19: (a) SEM image of x-ray sample-mask holder prepared using FIB milling. The objective and reference apertures are milled through both Au and Si_3N_4 layers; (b) schematic diagram of a cross-section of sample-mask. The specimen for x-ray imaging is typically mounted in front of the objective apertures. The reference apertures are drilled for holographic imaging. The reference apertures have conical shape with diameter of 300, 250 and 200 nm at the (Au) front side and 100, 75 and 50 nm at the (nitride) backside due to high-aspect-ratio milling.

Chapter 3

Red Blood Cell Preparation

3.1 Red Blood Cells Morphology

The main task of red blood cells (RBCs)[1] is to transport oxygen and CO_2. It fulfills this task as a passive transport vehicle in the circulating blood. The mature red cell has a biconcave-discoid shape with a mean diameter of 8 μm, a thickness of 1.7 μm and a volume of 83 μm^3 (See Figure 3.1(a)). The structure of the RBC is far from being settled and it has been a challenge over last century between scientists in different disciplines to come up with a model to satisfy all the experimental observations regarding different morphologies of the cells and various ways hemolysis[2] occurs [18]. One hypothesis suggests that the RBC has a balloon-like structure limited by a bilayer phospholipid membrane enclosing a solution of hemoglobin where the cytoplasm of the cell is more condensed at the cell's periphery and much less so in the interior [39].

The peculiar, bioconcave-discoidal, shape of the mammalian erythrocyte has intrigued many scientists in theoretical physics and clinical medicine ever since its first observation following the invention of sufficiently magnifying microscopes. While the basic perquisite for all non-spherical cell shapes is an excess in surface area produced by active removal of ions and water from the cytoplasmic compartment, it has become evident during the last century that the particular shape assumed by the mature mammalian erythrocyte is based on static and dynamic properties of the plasma membrane arising from the chemical composition, supramolecular organization and physical properties of its major components, lipids and proteins.

It has been known more than 50 years [19] that a variety of agents can modify the discoid shape of the RBC systematically and reversibly at constant area and volume. One set of agents, including anionic amphipaths, high salt, high pH, ATP depletion, cholesterol enrichment, and proximity to a glass surface, induces a series of crenated shapes, called echinocytes, characterized by convex rounded protrusions or spicules (see Figure 3.1[b-e]) [20]. Under further loading,

[1] Also referred to as "erythrocytes".

[2] Diffusion of hemoglobin out of erythrocytes is usually referred to as "hemolysis".

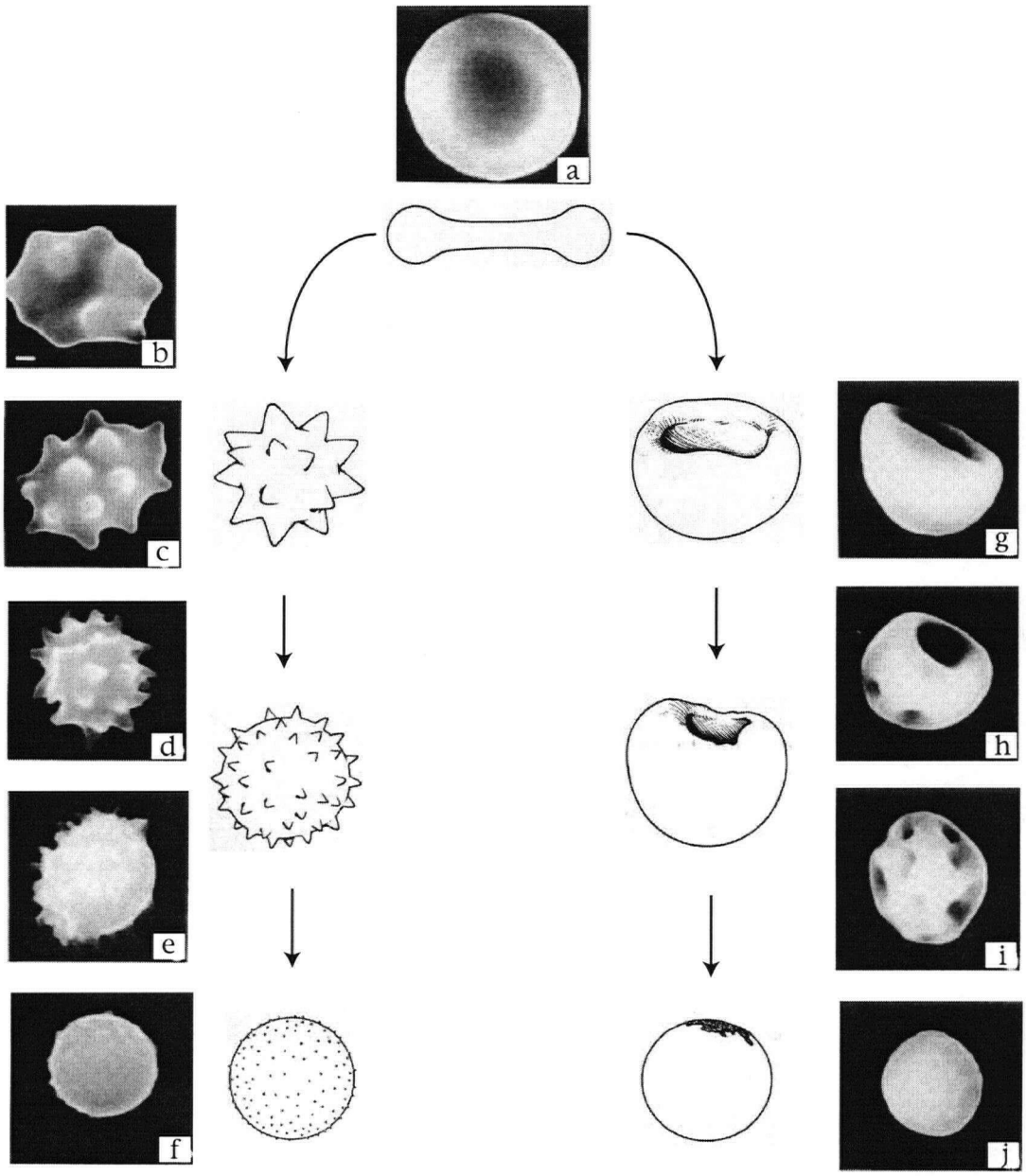

Figure 3.1: Scanning electron micrographs of a discocyte (a), echinocytes (stage +1 [b], stage +2 [c], stage +3 [d], stage +4 [e], stage +5 [f]), and stamatocytes (stage -1 [g], stage -2 [h], stage -3 [i], and stage -4 [j]). The scale bar in (b) is 1 μm. The scheme is modified from references [39, 40].

the spicules become smaller and more numerous and eventually bud off irreversibly, forming extracellular vesicles composed of plasma membrane materials and leaving behind a more or less spherical body with reduced area and volume (the spheroechinocyte, Figure 3.1[f]). Another set of agents, including cationic amphipaths, low salt, low pH, and cholesterol depletion, induces concave shapes called stomatocytes, (see Figure 3.1[g-h]) [20]. On further loading, multiple concave invaginations are produced, which eventually bud off to form interior vesicles and leave a spherostomatocyte, Figure 3.1(j). This main sequence is universal in the sense that the shapes seen and their order of appearance do not depend on which echinocytogenic or stomatocytogenic agent is used. This chapter includes a brief introduction to hemoglobin structure inside the RBC, along with discussion on the protocol used for fixing and mounting cells on the x-ray sample-mask structure, which is adaptable to imaging using both scanning electron microscopy and x-ray coherent scattering.

3.2 Hemoglobin as Dominant Protein inside RBC

Hemoglobin is the main intercellular protein of the red blood cell; it constitutes about 33% of the cell's contents. It has a molecular weight of 63,000 amu, and its assembled from four subunits so called polypeptide chains (two α globins composed of 141 amino acids and two β globin consisting of 147 amino acids), each of which contains a heme group in a hydrophobic pocket (see Figure 3.2) [41]. Each amino acid in the polypeptide chain is hydrogen-bonded to the amino acid that is four residues ahead of it in the chain. The hydrogen-bonding occurs between the H of an -NH group and the O of a -CO group of the polypeptide backbone chain.

The hemoglobin molecule undergoes conformational changes as it interacts with various ligands, including oxygen, hydrogen, carbon dioxide, and 2,3-diphosphoglycerate (2,3-DPG). In the deoxyhemoglobin form, beside the hydrogen bonding between amino acids along the polypeptide chains, the 2,3-DPG binds the two β chains to restrain the hemoglobin in a low-affinity form. In this configuration, the heme porphyrin is non-planar with the iron atom pulled out of the plane of the porphyrin toward the histidine residue[3] to which it is attached. This non-planar configuration comes from repelling of valence electrons surrounding the iron in the heme group and the valence electron in the histidine residue. When Fe binds to an oxygen molecule, the porphyrin ring adopts a planar configuration with Fe atom lying in the plane of the porphyrin ring. This leads to subtle shifts in histidine residue and attached amino acid chains toward the

[3]Histidine is an amino acid residue which links the heme porphyrin to the polypeptide chain.

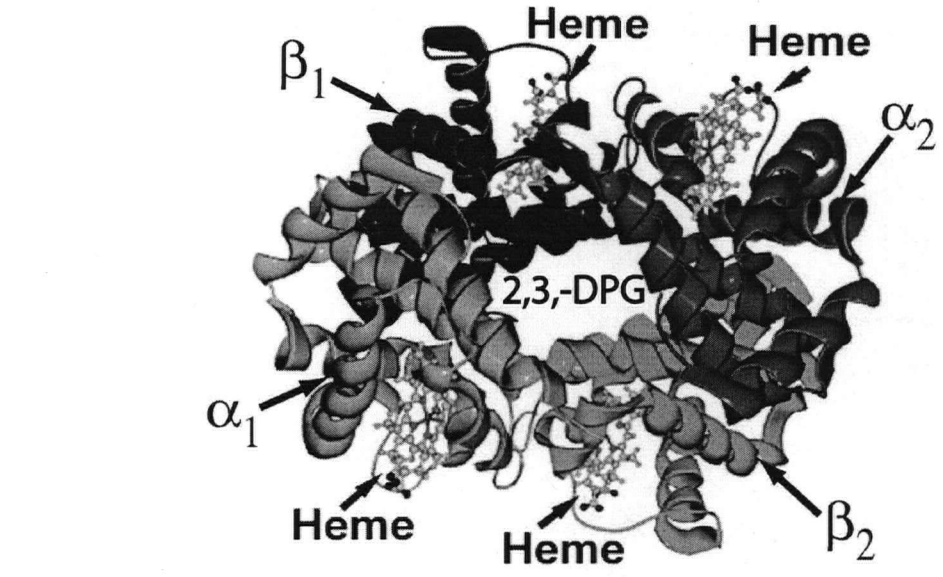

(a)

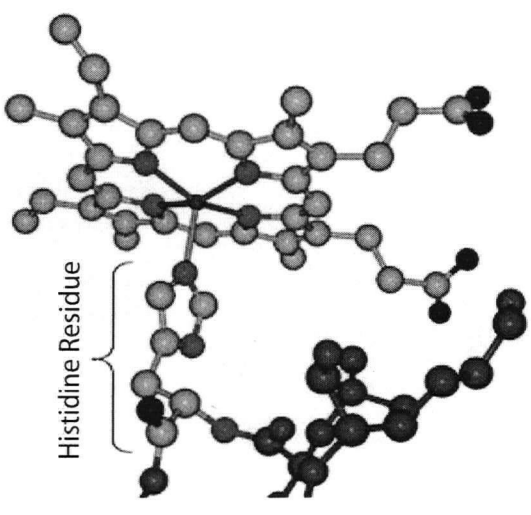

(b)

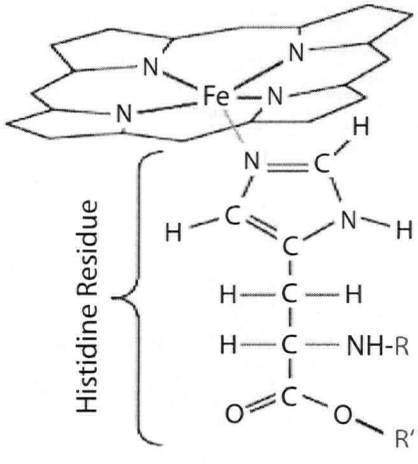

(c)

Figure 3.2: (a) Hemoglobin molecules are composed of four subunits: two α globins and two β globins, each of the globin chains provides a pocket for a heme molecule, therefore, has the capacity of binding up to four molecules of oxygen. 2,3,-DPG binds to the two β chains to stabilize the molecule when it is in the deoxygenated state; (b) a three-dimensional molecular model of heme coordinated to the histidine residue (a monodentate ligand) of the hemoglobin protein; (b) a two-dimensional drawing of heme coordinated to the histidine residue, which is part of the hemoglobin protein. In this figure, the protein is deoxygenated; i.e., there is no oxygen molecule bound to the heme group. Reprinted from reference [42].

porphyrin ring which is responsible for rupture of hydrogen bonds and apposition of the β chains to expel the 2,3-DPG and CO_2 from the crevice between them [42]. Thus upon binding one O_2 molecule, the whole protein changes its shape. In the new shape it is easier for the other three heme groups to bind three more O_2 molecules.

The high concentration of the hemoglobin in the RBC is so high as to be close to the crystallization point. Hemoglobin has been found to be in mesomorphic state[4] in all animal species [43]. The x-ray diffraction result from Dervichian et al. [44] has shown within the interior of a RBC there is a degree of organization intermediate between the relatively disordered state of an ordinary solution and the high degree of order encountered in the crystalline median. They observed that the hemoglobin molecules in erythrocytes were distributed so as to have an average distance of about 62 Å separating them.

In interpreting these observation, Finch et al. [45] suggested that hemoglobin inside the dried erythrocyte aggregates into long straight fibers. These may extend through most of the length of the cell, forming either square or hexagonally packed bundles with lattice constants of 17 - 18 nm. Each fiber is a tube made up six thin filaments, which are wound around the tubular surface with a helical pitch of about 300 nm. Each filament is a string of single hemoglobin molecules linked end to end at intervals of 62 Å . The molecules in neighboring filaments are arranged so that they form flat hexagonal rings; these rings are stacked so that successive ones are rotated about the fiber axis by 7.2° (See Figure 3.3). This model leads precisely to the periodicity of 62 Å found by Dervichian [44]. Thus, in the RBC, hemoglobin molecules exist at a concentration that will just permit their free rotation.

3.3 Preservation of RBC Microstructure using Fixatives

One purpose of fixation is to maintain cells as close as possible to their original in vivo condition with regard to volume, morphology, and spatial relationships of organelles and macromolecules. The main emphasis in fixation studies has been concentrated on the effects of fixatives for light and electron microscopies [46–48]. A complete study of basic cell membrane changes during and after fixation has been presented in references [49, 50]. It is suggested that fixation alters the permeability of the cell membrane and probably the osmotic behavior of the cell [49, 50]. The

[4] A state of matter in which the degree of molecular order is intermediate between the perfect three-dimensional, long-range positional and orientational order found in solid crystals and the absence of long-range order found in isotropic liquids, gases, and amorphous solids.

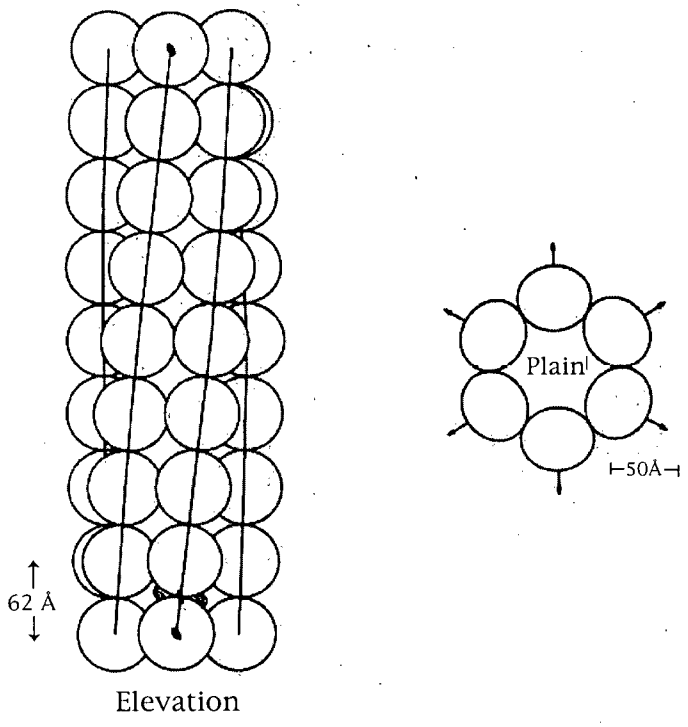

Figure 3.3: Structure of helical tube of hemoglobin inside the red blood cells. The arrows and signs indicate the probable positions of the molecular dyads normal to the fiber axis. A length of eight rings is shown corresponding to the approximate repeat of the structure. Reprinted from reference [45].

most commonly used fixative solutions used for RBCs in electron microscopy are glutaraldehyde (GA) and osmium tetroxide (OsO_4). The chemical mechanism of fixation with GA is different from that with OsO_4. GA acts mainly as a protein cross-linking agent, whereas OsO_4 reacts mainly with lipids [49, 51, 52], and this difference may result in differing stability of the cells. We used a similar protocol to the one used commonly for electron microscopy, which involves initial fixation with GA followed by post-fixation by OsO_4. This allows us to capture SEM images of the erythrcytes before and after x-ray imaging without any modification to the cell's microstructure.

The blood samples were drawn from the author using a silicone-coated syringe and stored in a centrifuge tube at room temperature. The sample was spun at 4000 RPM (mean radius of gyration of 10 cm) for 20 minutes at 20°C. After centrifuging the supernatant plasma and buffy layer (white cells) were removed. The remaining RBC were transfered to a plastic vial containing 2.5% GA in 0.1 M sodium cacodylate buffer. The pH of the solution was adjusted to 7.4. This

solution was kept at room temperature for 3 hours. The solution was centrifuged again and the RBCs were extracted from the solution and washed three times with 0.1 M Na-cacodylate buffer and transfered to 2% OsO_4 solution in NA-cacodylate solution for post-fixation. After 1 hour fixing in the Osmium solution, the cells were washed four times with 0.1 M phosphate buffer saline (PBS) and stored in 50% ethanol solution. At this stage the cells were ready to be mounted on the x-ray sample-masks.

3.4 Mounting of the cells on the x-ray sample-mask

The mounting of the cells on the x-ray sample-mask was done in Evan Evans lab in UBC hospital. A schematic of the complete instrumental assembly is shown in Figure 3.4. Sample chambers were made of two cleaned glass coverslips glued with vacuum grease and sealed with nail polish to an stainless steel support (1-mm thickness). The x-ray sample-mask is positioned inside the sample chamber with the silicon nitride side face up (see Figure 3.5). Then the chamber is filled with 50% ethanol solution. After the substrates settle down at the bottom of meniscus the solution of fixed RBC inside 50% ethanol solution is injected and dispersed in the chamber.

The silicon nitride surface is generally hydrophobic which causes the substrate to float on the meniscus of the ethanol. This makes the task of mounting the RBCs very difficult, since the substrates won't stay steady. To change the surface from hydrophobic to hydrophilic, the substrates were treated with an oxygen plasma. In the plasma surface treatment electrons, ions, atoms, and radicals attack the surface of the substrate. This process extracts hydrogen atoms from the substrate surface to form radical sites, and then oxygen atoms react with the radicals to form oxygen functionalities including OH, C=O, and COOH groups [53]. The substrates were exposed to oxygen plasma with RF power 150 W for 20 seconds. A longer period of time causes the silicon nitride to be etched. This treatment is not permanent; if the substrates are exposed to the atmosphere, due to adhesion of organics from the atmosphere the surface returns to a hydrophobic state. The hydrophilic state lasts less than 30 minutes in air. Thus the substrates were cleaned just before placing them inside the sample chamber, and were kept inside closed container filled with Ar at all times.

The sample chamber is positioned on the stage of an inverted microscope (Zeiss Axiovert). The microscope was equipped with a 100× Plan-Achromat oil objective (1.4 NA), a 0.8 air NA condenser, and a 200 W mercury arc lamp. The transmission bright-field images were either collected by an analog CCD camera (XC-ST70CE, SONY) and recorded at 30 frames/s after

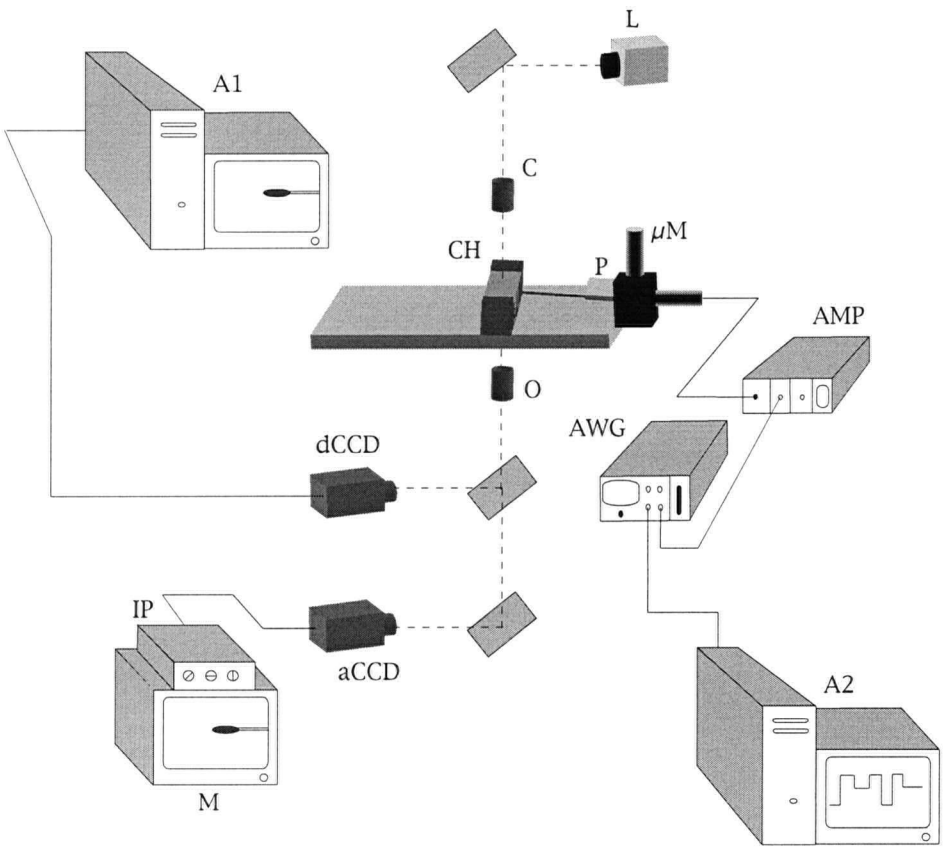

Figure 3.4: Schematic of micromanipulation apparatus used for mounting RBCs on x-ray sample-mask. Complete instrumental apparatus assembled around a bright-field inverted microscope. Light from mercury arc lamp **L** travels through condenser **C** and illuminates the sample. Objective **O** collects the images which can be captured either by fast-rate (100 fps) digital camera **dCCD** and stored by computer **A1** or by anlalog camera **aCCD** (25 fps), visualized on control monitor **M** after image processing **IP**. Simultaneously, the arbitrary waveform generator **AWG** controlled by computer **A2** via GPIB interface provides the input signal to high-voltage amplifier *Amp* which drives piezo element **P**. Piezo translator **P** is mounted on three-axis motorized micromanipulator μ**M** and sets the cell-holding micropipette displacement.

contrast enhancement (Argus image processor, Hamamatsu, Shikzuoka, Japan) or captured by a digital monochrome CCD camera cooled to -30°C (Sensicam, PCO, Kelheim, Germany) at video rates of 100 frames/s using dedicated image analysis software. Manipulation and alignment of the erythrocytes were done using a micropipette. To do so, the micropipette was mounted on a mechanical three-axis microtranslator on the side of the microscope stage. The movement of the micropipette is controlled by a piezoelectric translater (5μm travel stacked piezo, Physik

Instruments, Waldbronn, Germany). Control of the piezo was performed through an arbitrary waveform generatior (GA 1241, Thurlby Thandar Instruments, Huntingdon, UK) which was programmed via GPIB interface in a LabView (National Instruments) environment. This setup is commonly used to probe molecular adhesion and structural linkages at biological interfaces. A detailed description of the setup is provided in reference [54]. This apparatus made it possible

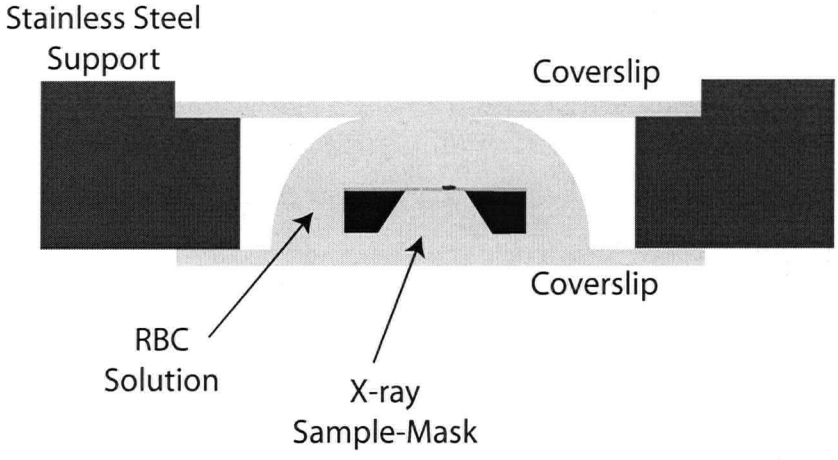

Figure 3.5: Schematic of sample chamber which is consist of two cleaned glass coverslips glued with vacuum grease and sealed with nail polish to an stainless steel support (1-mm thickness). The x-ray sample-mask is positioned with the nitride facing up.

to selectively choose specific erythrocytes with a particular shape and mount it in front of the objective aperture on the x-ray sample-mask structures. The adhesion of the RBC to clean silicon nitride surface through electrostatic forces is rather strong. We noticed that the mounted cells on the substrate stayed intact after flushing the substrates a few times with 50% ethanol solution. At this step, there is still residual water and ethanol inside the cell . The drying of the cells in air or vacuum can drastically change their microstructure and possibly destroy them completely. The surface tension of water in a cell at the point at which it changes from the liquid phase to the gaseous phase can destroy the cell. By increasing the pressure and temperature of the cell to the critical point (CP) it is possible to dry it without crossing a phase boundary. This is possible because once the CP has been passed, the density of the liquid and the density of the gas are the same. The CP for water is 228.5 bar and 374°C. However this high pressure and extreme temperature most likely destroys the cells, for this reason the cells must first be treated in a suitable transitional fluid such as CO_2 whose CP is 73.8 bar and 31°C.

The x-ray scattering experiments are usually carried out inside a high vacuum chamber (10^{-6} - 10^{-7} torr). Thus the RBCs need to be dehydrated properly before being transfered to the scattering chamber. The dehydration was done by washing the cells through a series of increasing ethanol concentrations up to 100% ethanol followed by critical point drying. We used ethanol solutions of 50, 70, 90, 95 and two stages of 100 % ethanol. Then the samples were transfered to a Balzer 020 CPD. The first step, namely the replacement of the ethanol inside the cells with liquid CO_2, is done at 10°C, then the liquid CO_2 is converted to the gas phase by passing through the critical point of CO_2. After the critical point drying the samples were stored in a dry plastic sample box with some desiccant material. As long as the samples are kept in a dry environment and not exposed to moisture the cells can last for years and can be introduced to any high vacuum chamber without changing their microstructure.

Chapter 4

X-ray Coherent Scattering from Red Blood Cell

4.1 Lensless Imaging Using Coherent X-ray Scattering

In lensless imaging instead of collecting the scattered intensity from the small sample with an objective lens as in a conventional microscope, the scattered intensity is recorded on a screen behind the sample. The advantages of this technique are eliminating any aberration from lenses, eliminating the need for a lens, simplicity of the optical setup and achieving spatial resolution up to the maximum photon momentum transfer. In the experiment one measures the intensity of the scattered wave field rather than recording the phase and amplitude separately. The main challenge is to retrieve the lost phase information of the scattered electric fields from the intensity measurement. Coherent x-ray imaging requires two conditions to be fulfilled: (a) illumination of the sample with a laterally coherent beam and (b) the maximum path length difference (i.e. sample thickness) has to be smaller than the longitudinal coherence length $\xi_l = \lambda^2/2\Delta\lambda$ [55]. The first condition is usually satisfied by using a pinhole of diameter, d, as a spatial filter, where the transverse coherence length is given by:

$$\xi_t = \frac{z\lambda}{2\pi d}. \tag{4.1}$$

where z is the center-to-center distance between the pinhole and the sample. Thus in order for the scattering to be fully coherent in the transverse direction, the object width S should be smaller than the transverse coherence length ξ_t.

For coherent electromagnetic waves propagating through an object, phase differences arise between different parts of the wavefront. These are due to spatial variations in the refractive index of the object, which for x-ray wavelengths is given by

$$n = 1 - \delta + i\beta. \tag{4.2}$$

Here, $\beta = \mu\lambda/4\pi$ describes the absorption of the x-rays with $\mu(\mathrm{m}^{-1})$ the absorption coefficient. This term causes the amplitude of the transmitted waves to decay. The term

$$\delta = \frac{\lambda^2 r_e}{2\pi}\rho(\mathrm{r}), \tag{4.3}$$

with $r_e = 2.818 \times 10^{-15}$ m, the classical radius of the electron, and $\rho(\mathrm{r})$ the electron density of the material, affects the phase of the waves. As an example Figure 4.1 shows a plot of δ and β for PMMA as a function of energy in the soft x-ray regime. Thus the phase contrast dominates the absorption contrast in this x-ray regime. The advantageous of being sensitive to phase contrast is that even small spatial variations in the refractive index can be detected.

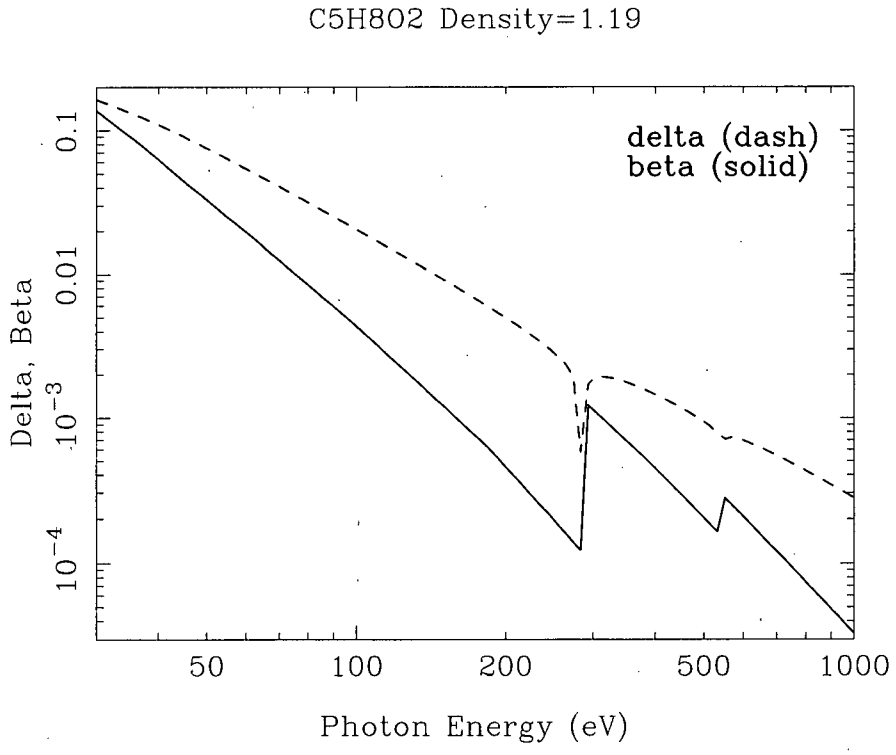

Figure 4.1: Refractive index component for PMMA in the soft x-ray region reprinted from [56].

The structural detail in a phase contrast image depends on the distance L between the object and the detector which defines the diffraction regime. Here, we consider diffraction in the Fraunhofer limit where the sample-to-detector distance, $L \gg S^2/\lambda$, where S is the largest lateral dimension of the sample and λ is the wavelength of the light. We consider a plane wave incident on a planar object with transmission function $t(X, Y)$ (See Figure 4.2). The diffracted

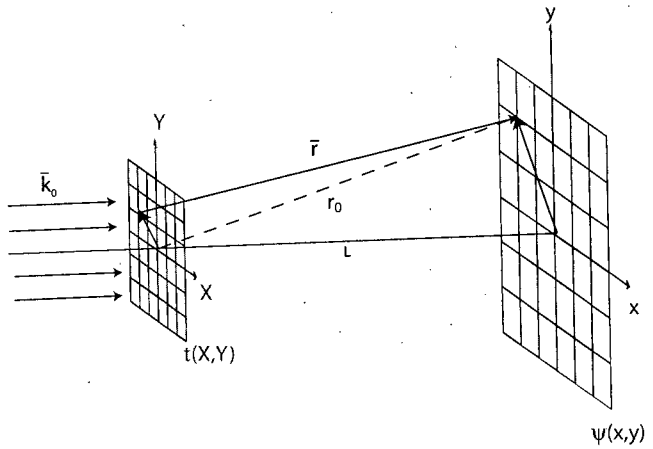

Figure 4.2: Propagation of a plane wave through a planar object with transmission function $t(X,Y)$. Angles and distances are not to scale.

amplitude in the (x,y) detector plane at distance L is found by considering each infinitesimal surface element $\mathrm{d}x\ \mathrm{d}y$ in the object plane to be a secondary source of spherical wavelets and by summing over the total area [57]:

$$\psi(x,y) = \frac{i}{\lambda}\int\int t(X,Y)\frac{\exp(ikr)}{r}\mathrm{d}X\mathrm{d}Y. \tag{4.4}$$

where the radial distance r is the length of the vector conecting the point (x,y) with (X,Y) which is given by:

$$\begin{aligned} r &= \left[L^2+(x-X)^2+(y-Y)^2\right]^{1/2} \\ &= \left[r_0^2-2xX-2yY+X^2+Y^2\right]^{1/2}. \end{aligned} \tag{4.5}$$

Since $L, r_0 \gg x, X, y, Y$, we expand r in the exponent of Eq. 4.4 up to second order around r_0 and obtain:

$$\psi(x,y) = \frac{i\exp(ikr_0)}{\lambda}\int\int t(X,Y)\exp\Big(-ik\frac{xX+yY}{r_0}\Big)\exp\Big(-ik\frac{X^2+Y^2}{2r_0}\Big)\mathrm{d}X\mathrm{d}Y. \tag{4.6}$$

The transmission function can be represented by a phase factor [58]

$$t(X,Y) = \exp[i\phi(X,Y)], \tag{4.7}$$

with $\phi(X,Y)$ equal to $(2\pi/\lambda)\times$ (the optical path length difference) over the sample thickness $l(X,Y)$, projected onto the (X,Y) plane:

$$\phi(X,Y) = \frac{2\pi}{\lambda}\int_0^{l(X,Y)}\Big[\delta(X,Y)+i\beta(X,Y)\Big]\mathrm{d}Z, \tag{4.8}$$

where the second term in the integrand is the absorption. If $\phi(X, Y)$ is real and small, the object is said to be a weak phase object [57], and one can approximate the exponent in Eq. 4.7 by

$$t(X, Y) \approx 1 + i\phi(X, Y). \tag{4.9}$$

The exponent in the second exponential term in Eq. 4.6 results from the spherical curvature of the wavefronts. The curvature becomes negligible for $r_0 \simeq L > S^2/\lambda$, with S the sample size ($S \approx \max[X, Y]$). Hence the second exponential term becomes unity, and the diffracted amplitude is the Fourier transform of $t(X, Y)$; also the amplitude distribution $\psi(x, y)$ does not change shape with increasing distance.

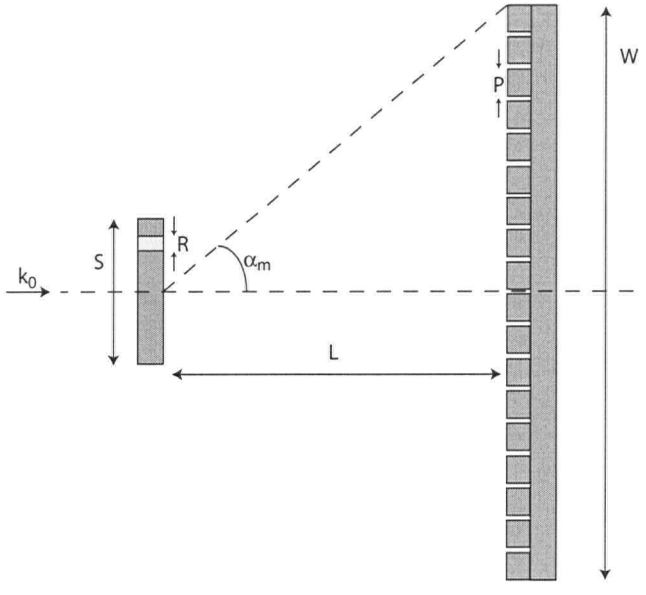

Figure 4.3: Geometrical parameters of importance for resolution and oversampling in a coherent scattering experiment; incident wave vector (k_0); sample size (S); smallest resolvable element (R); sample-detector distance (L); detector size (W); detector pixel size (P).

For coherent scattering in transmission through a sample at normal incidence, the longitudinal coherence length, ξ_l, limits the maximum scattering angle α_m to $\sin\alpha_m < \xi_l/S$, where S is the transverse sample size (see Figure 4.3) [55]. Defining R as the smallest resolvable element in the object plane which is determined by $2\pi/q_{\|}^{max}$ where $q_{\|}^{max}$ is the maximum momentum transfer in the object plane. In the given geometry for small angle scattering, the wavelength (λ), the

sample-detector distance (L) and the detector size (W) determine the resolution,

$$R = \frac{2\lambda L}{W}. \tag{4.10}$$

Diffraction from disordered media leads to the formation of speckle patterns with individual speckle sizes proportional to $\lambda L/S$. The oversampling Ω_{2D} refers to the ratio of the individual speckle size over the pixel spacing, P. We have [59]:

$$\Omega_{2D} = \left(\frac{\lambda L}{SP}\right)^2. \tag{4.11}$$

As higher oversampling increases redundancy, an oversampling larger than two is desirable [60]. Thus in designing a coherent x-ray scattering experiment one should pick the detector to sample distance with the given detectors pixel spacing such that individual speckles span over a few pixels to achieve higher oversampling. For a given oversampling factor, the resolution is thus coupled to the maximum field of view given by the sample size according to

$$\Omega_{2D} = \left(\frac{RW}{2SP}\right)^2. \tag{4.12}$$

Hence, the effective sample size can be limited by the illumination size.

4.2 X-ray Speckle Simulation on Microfabricated X-ray Sample-Mask

In Sec. 2.2.2 we showed experimental results on microfabrication of circular apertures using FIB milling. It remains to investigate the changes in the scattered intensity rising from roughening of the sidewall and the bottom of the aperture. The input to the speckle simulation is an AFM image of a 5 μm diameter hole milled using FIB. The geometry of the simulation is shown in Figure 4.2. The AFM image is used as the transmission function $t(X, Y)$ where the transmission at each pixel point is determined using x-ray transmission data available in reference [56]. The thickness of the silicon nitride membrane is estimated to be 100 nm and any higher thickness is taken to be residual gold with the correct transmission for gold at the given energy. The diffracted amplitude in the (x, y) detector plane is calculated using Eqs. 4.4 in the discrete form as:

$$\psi(x_n, y_m) = \sum_{N_X=0}^{N-1} \sum_{N_Y=0}^{N-1} t(N_X\Delta X, N_Y\Delta Y) \frac{\exp\left(ik_0 r(x_n, y_m)\right)}{r(x_n, y_m)} \Delta X \Delta Y, \tag{4.13}$$

where the radial distance $r(x_n, y_m)$ is given by:

$$\begin{aligned} r(x_n, y_m) &= \left[R^2 + (x_n - N_X \Delta X)^2 + (y_m - N_Y \Delta Y)^2\right]^{1/2} \\ &= \left[r_0^2 - 2x_n N_X \Delta X - 2y_m N_Y \Delta Y + (N_X \Delta X)^2 + (N_Y \Delta Y)^2\right]^{1/2}. \end{aligned} \quad (4.14)$$

here N_x, N_y determine the pixel lengths in the X and Y directions in the object plane. In an AFM image captured with 512 × 512 pixel resolution, therefore $N_X = N_Y = 512$. The values ΔX and ΔY correspond to the pixel spacing in the X, and Y direction in the AFM image (scan range / number of pixels), which in this case was 6.5 μm / 512 = 13 nm/pixel. The wavevector, k_0 of the incident x-ray with energy E is given by, $k_0 = E/\hbar c$. The variables x_n and y_m in the detector plane are given by $x_n = n\delta x$ and $y_m = m\delta y$ where δx and δy are the pixel spacing in the detector plane; n and m are the pixel length in the x and y direction in the detector. We used the values for the actual detector used in the experiments which was 2048 × 2048 pixel with a pixel spacing of 13.5 μm. The object and detector spacing, L, is 315 mm.

The results of the speckle simulation on three different apertures at E=708 eV are shown in Figure 4.4. The perfect circular apeture with straight sidewall and flat bottom has the well-known Airy pattern intensity distribution [57]. As we add the roughness to the bottom of the aperture, Figure 4.4(c) the overall intensity distribution decreases along with some angular distribution changes, i.e. forming speckles having sizes proportional to $\lambda L/S = 110$ μm where S is the diameter of the aperture and L is sample-to-detector distance. The intensity distribution across individual speckle comes from the roughness characteristic length in the bottom of the aperture. There is much stronger disturbance in the diffraction rings in the case of rough sidewall aperture in Figure 4.4(e). The speckle sizes are the same as in the former case however the strong scattering of the edges causes larger intensity modulation among individual speckles. In this case the speckle intensity distributions are proportional to the roughness characteristic of the sidewall.

In Figure 4.5(a-c) we have plotted the boxed area in diffraction patterns of Figure 4.4 to see the changes in the diffraction pattern more closely. There is some disorders in the diffraction rings from the perfect circular aperture which directly comes from digitization of a circular aperture. In conclusion the roughening of the sidewall causes much more drastic changes in the speckle pattern and introduces non-desirable noise to actual data. In practice one can deconvolve this effect from the actual pattern in a rather rigorous way [61]. Thus producing circular apertures with smooth sidewalls using FIB milling is very valuable toward higher resolution imaging.

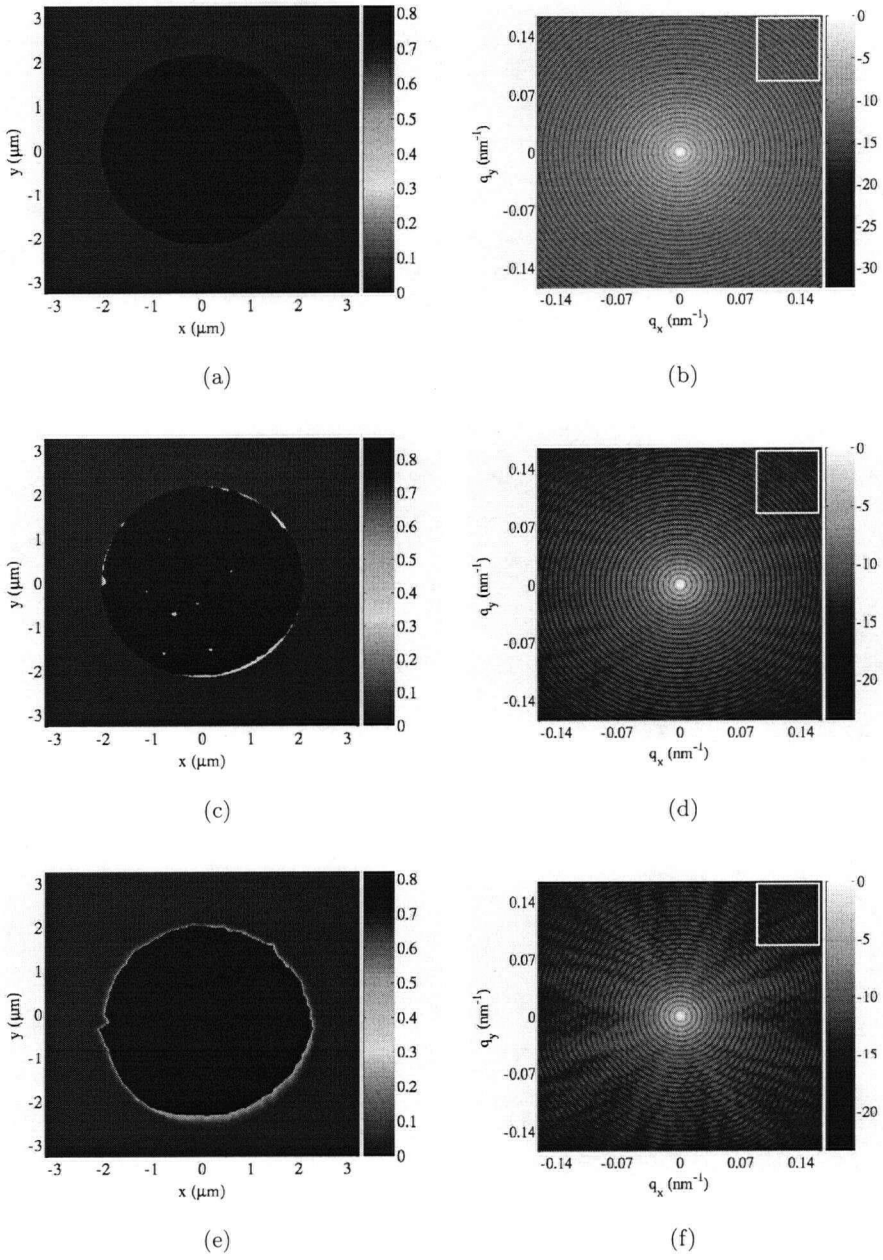

Figure 4.4: Speckle simulation on circular apertures with different characteristics microfabricated with FIB milling: (a) Perfect circular aperture made digitally as a reference; (c) circular aperture with straight sidewall and bottom roughening due to FIB milling instability; (e) rough sidewall aperture with flat bottom. The right column is the corresponding scattered intensity calculated using the speckle simulation.

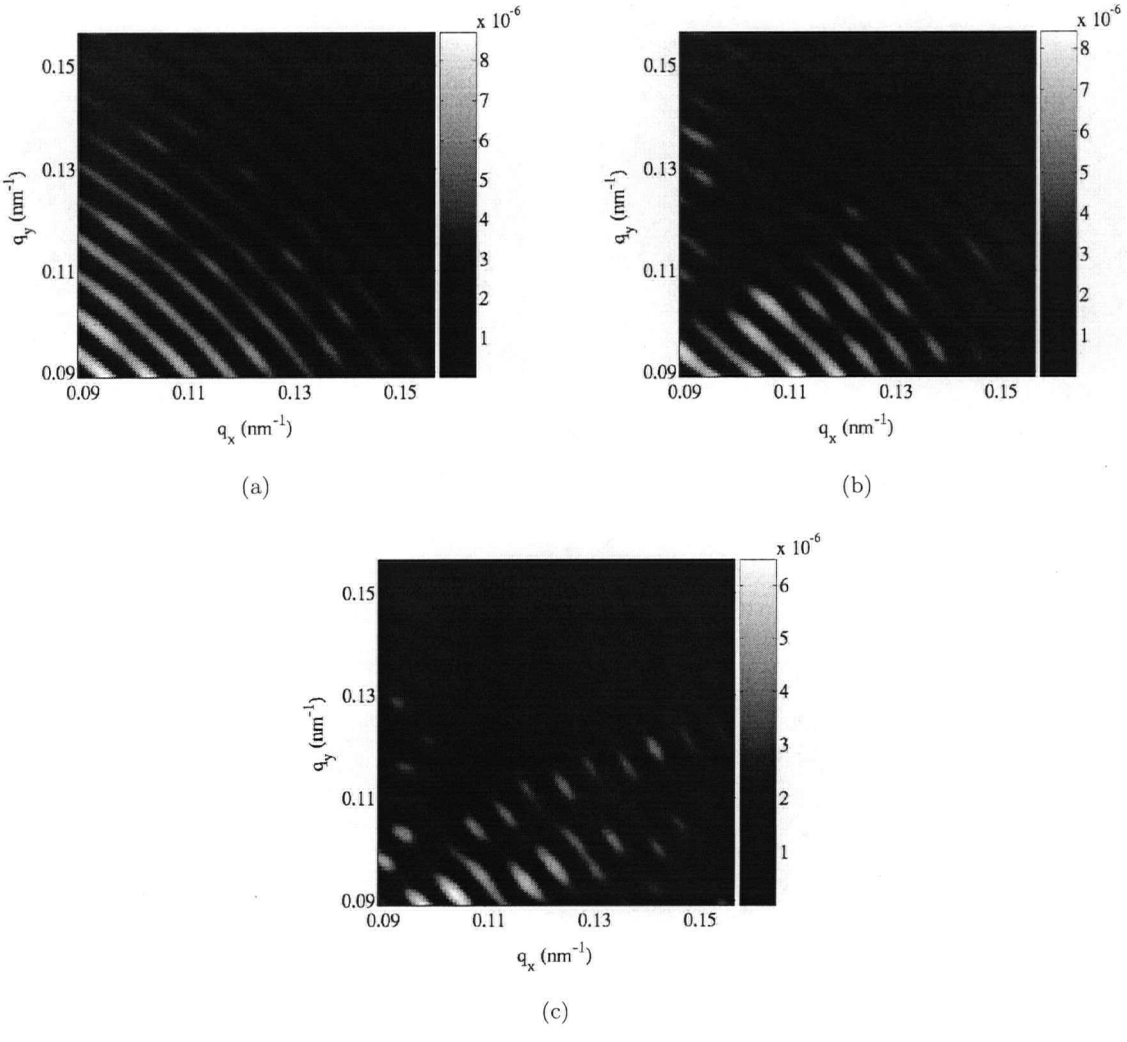

Figure 4.5: Magnified scattered intensity distribution of the boxed area in Figure 4.4. Scattered intensity from a (a) perfect circular aperture; (b) circular aperture with straight sidewall and bottom roughening; (c) rough sidewall aperture with flat bottom. There is some disorder in the diffraction rings from the perfect circular aperture (a) which directly comes from digitization.

4.3 Coherent Soft X-ray Scattering Experiment

Experiments were performed at the UE52/1-SGM beamline at BESSY II, Berlin. The beamline uses the x-ray synchrotron radiation generated in a helical undulator. The polarization of the emitted radiation can be varied from linear (in any direction perpendicular to the beam) to positive and negative circular. In our experiment, the third and first harmonics of the undulator output is further monochromatized in the beamline to provide soft x-rays tuned to Fe L_3- and C K- absorption edges respectively. The monochromator resolution is estimated to be on the order of $\lambda/\Delta\lambda = 4000$ for the slit setting used in our experiment.

Details of the beamline are depicted in Figure 4.6. In the broad outline the beamline consists of pre-focussing optics, a monochromator and re-focussing optics. The pre-focussing optics, a horizontally deflecting cylindrical mirror, focuses the undulator beam vertically onto an entrance slit. Further downstream an off-axis rotatable plane mirror in front of the grating allows for a variation of the deviation angle at the grating and hence a precise fulfillment of the focussing condition [62]. Interchangeable gratings (900, 1200, and 1500 lines/mm) were installed to cover a broad energy range with a very high energy resolution and high efficiency. For an energy scan the rotation of the grating and the plane mirror are the only motions of the beamline components. The rotations are controlled in-situ and on-axis by UHV-compatible angle encoders [63] with an angle resolution of less than 0.001 arcsec. The re-focussing optics consist of a horizontally deflecting cylindrical mirror for vertically imaging the exit slit to the sample position and a horizontally deflecting plane ellipse for a strong horizontal demagnification (47:1) of the relatively large horizontal source size ($\approx$ 700 μm FWHM). The beam divergence at the focus was 6 mrad (hor.) x 1 mrad (ver.) with a spot size of 17.4 μm (hor.) $\times$ exit slit size (ver.).

The ALICE diffractometer end station shown in Figure 4.7 was used for the scattering experiment. The diffractometer consist of a two-circle goniometer in a cylindrical vacuum chamber with a 400 mm inner diameter and a 310 mm height with the cylindrical axis vertical. The diffractometer operates in a horizontal scattering geometry. The chamber is high vacuum (HV) compatible and can reach a base pressure of 1×10^{-7} torr using a turbomolecular pump, backed by a scroll-type dry roughing pump. The sample can be changed through a 200 mm diameter loadlock window. The sample is cooled by a closed-cycle He cryostat that provides a working temperature range of 2 - 600 K. A magnetic field of up to 0.5 T can be applied. The scattered intensity is measured using a Hamamatsu GaAsP photodiode.

For x-ray coherent scattering measurements the photodiode detector is moved out of the

beam direction and a 2048 × 2048 pixels soft x-ray charge-coupled device (CCD) from Princeton Instruments (PI-SX) with 13.5 μm pixel size is installed in the forward direction. Rather than using a pinhole at a focus of the beam for transverse coherence filtering, the sample was positioned significantly behind the focus in order to obtain sufficient spatial coherence. The sample-mask structure with the RBC attached was mounted on an aluminum frame of dimension 10 mm × 10 mm using silver epoxy and the whole sample assembly was mounted on the end of the copper holder inside the ALICE chamber. The geometry of the transmission scattering geometry is shown in Figure 4.8. Given the sample distance from the detector (315 mm) and detector size of 27.6 mm × 27.6 mm we can calculate the in plane momentum transfer and ultimately the final resolution. Defining the momentum transfer as

$$\mathbf{q} = \mathbf{k_f} - \mathbf{k_0}, \tag{4.15}$$

where $\mathbf{k_0}$ and $\mathbf{k_f}$ are the incoming and outgoing wavevectors, we write $\mathbf{q}_{\|} = (q_x, q_y)$ as the parallel (to the surface) component of the total momentum transfer and q_z as the perpendicular component. In this experiment, considering the geometry, the parallel momentum transfer $q_{\|} = \sqrt{{q_x}^2 + {q_y}^2}$ spans up to a maximum of $q_{\|}^{max} = \frac{2\pi}{\lambda} \sin\alpha_m = 220\mu\text{m}^{-1}$ where $\lambda = 1.77$ nm at the Fe L_3-edge and $\alpha_{max} \sim \sqrt{2} \cdot 13.8/315$ is determined by the size of the detector and its separation from the sample. The resolution is limited by $2\pi/q_{\|}^{max} \sim 28$ nm. Repeating the same calculation near the C K-edge, one finds a maximum resolution of 70 nm.

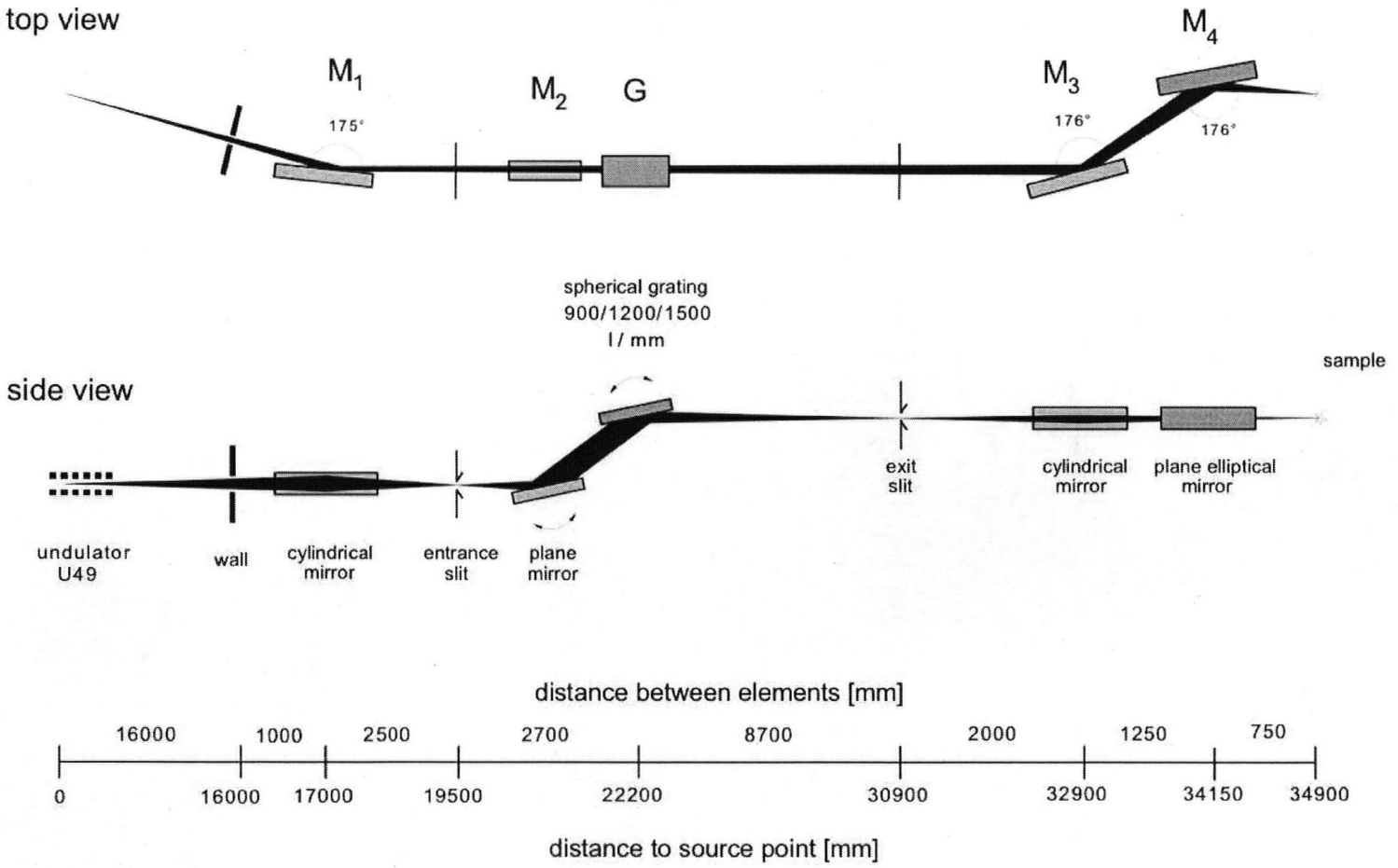

Figure 4.6: Schematic of UE52/1-SGM Beamline at BESSY II.

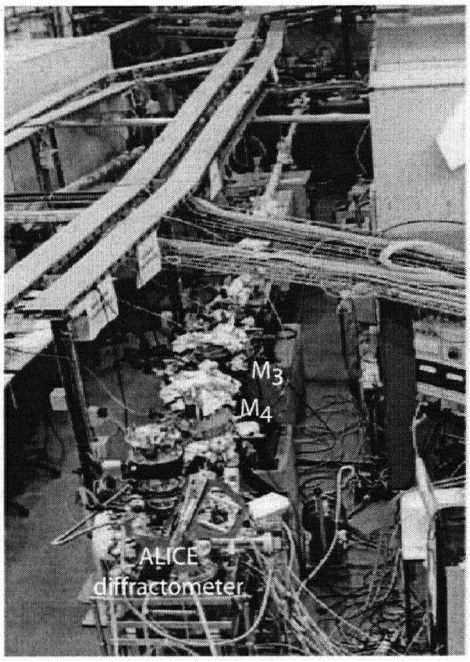

(a)

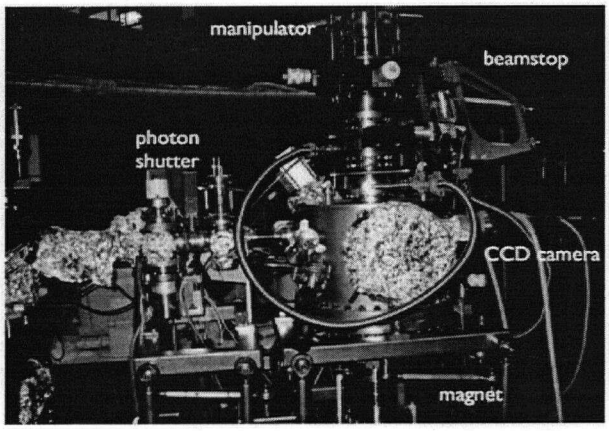

(b)

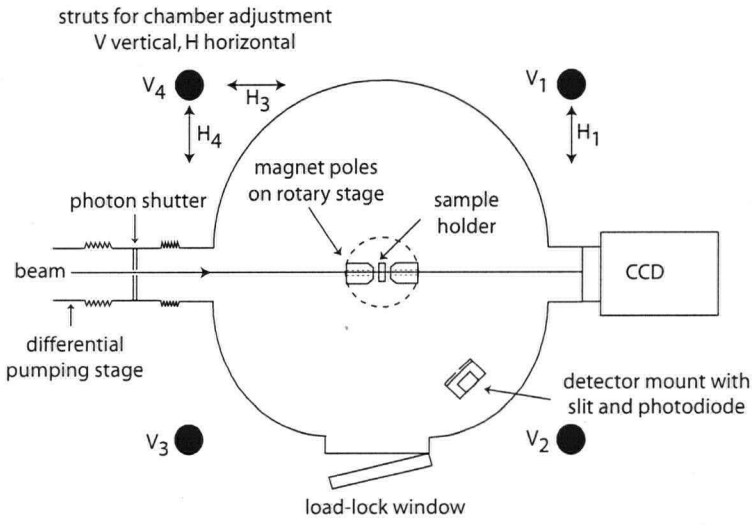

(c)

Figure 4.7: (a) overview of the beamline UE52/1-SGM at BESSY II; (b) ALICE diffractometer; (c) schematic top view of ALICE diffractometer reprinted from [64].

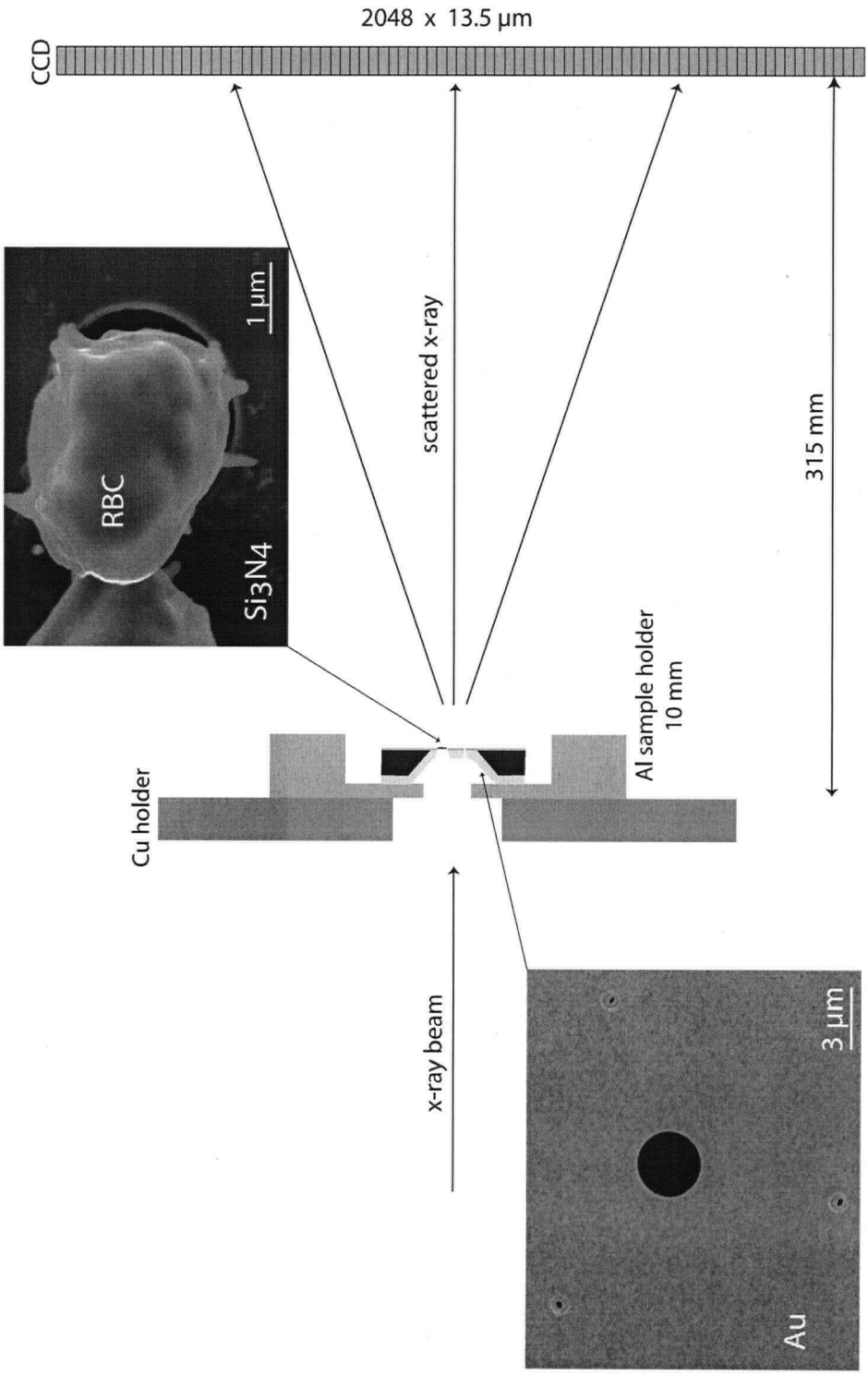

Figure 4.8: Side-view of experimental scattering geometry.

4.4 Experimental Results

The experiment was first performed near the Fe L_3-edge, $E = 706.7$ eV in order to investigate the sensitivity of the scattered intensity to the presence of Fe in hemoglobin inside the RBC. Figure 4.9(a) shows the scattered intensity recorded from sample RBC5 at $E = 707$ eV. In this sample the objective aperture is about 3 μm with three reference holes with diameters of 300, 250 and 200 nm on the gold side at 9 μm center to center distance from the object hole. Due to high aspect ratio milling through the gold layer the holes appear tapered with diameters 100, 75 and 50 nm on the nitride side respectively. In order to record higher photon counts at large scattering angles on the CCD while at the same time avoiding pixel saturation at the center we used a beam-stop at the center of the speckle pattern. The beam-stop was an epoxy drop 200 μm x 100μm on top of a 20 μm thick copper wire. After the measurement the pixels which were masked by the beam-stop were corrected by the corresponding values from the speckle simulation of the SEM image of the RBC5 sample (See Figure 4.9(b)). The scattered intensity was recorded for 1 second exposure time per frame. To improve the counting statistics fifty image frames were accumulated. The largest intensity is found in the vicinity of the center, corresponding to the specular direction. For better visibility of the weaker structures, the color z scale has been saturated for the central beam. The Fraunhofer diffraction rings due to the aperture are clearly visible. A high frequency oscillation created by the interference of the object and the reference waves is visible with high contrast. The individual speckles size was about $\lambda L/S = 64.5$ μm with the given 13.5 μm pixel spacing on the detector. This leads to oversampling of 4.8 along each direction. The dynamic range of the interference pattern is defined by the ratio of the background noise to the maximum intensity, which is found to be 10^6. The transmission through 800 nm thick gold film at E = 707 eV is about 10^{-4} % and through 100 nm Si_3N_4 it is 82 %. However in the interference pattern near the center we can see asymmetric bright intensity which directly comes from x-ray transmission through the gold mask and Si_3N_4. In practice one can eliminate this by coating the Si_3N_4 substrates with a thicker gold films.

The presence of the reference holes on the sample-mask structure leads to Fourier transform spectro-holographic imaging as described by Eisebitt et al. [21]. The reconstruction of the holographic image can be understood as follow. The electric field of the aerial image centered in the objective aperture is written as $t(X, Y)$. Propagating this field to the CCD plane located in the far field yields $T(x, y)$. Similarly $R_n(x, y)$ is the far field propagation of $r_n(X, Y)$, which is simply a point source representing the reference apertures. Since the far-field Fraunhofer

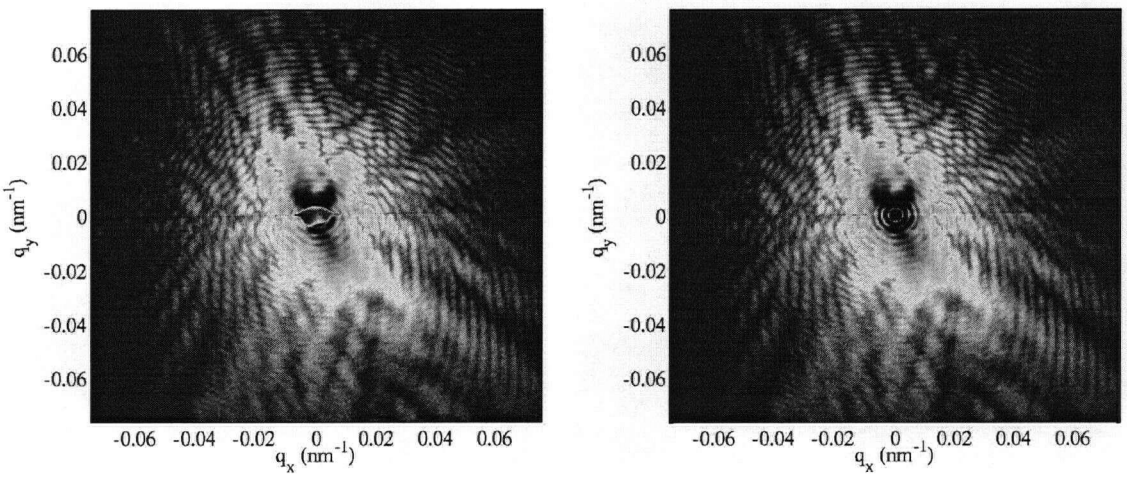

Figure 4.9: Measured scattered intensity at $E = 707$ eV (a)with the beam-stop blocking the central peak of the Airy pattern; (b) corrected image using speckle simulation from the top SEM image in Figure 4.8. The maximum momentum transfer in the measurement was ± 0.156 nm^{-1}, shown up to ± 0.078 nm^{-1} in the image. Intensity is represented on a logarithmic color scale, with blue denoting the minimum intensity 10^2 and red denoting the maximum intensity of 10^6. For better visibility of the weaker structures, the color z scale has been saturated for the central beam. The dynamic range of the interference pattern is 10^6.

diffraction is related to the Fourier transforms [65], $T(x, y)$ and $R_n(x, y)$ are Fourier transforms of $t(X, Y)$ and $r_n(x, y)$, respectively. Therefore the intensity pattern recorded at the CCD can be written as [65]:

$$\begin{aligned} I_{CCD}(x,y) &= \left| T(x,y) + \sum_{n}^{N_R} R_n(x,y) \right|^2 \\ &= T \times T^* + \sum_{n}^{N_R} R_n \times R_n^* + \sum_{n,m}^{n \neq m} R_n \times R_m^* + \sum_{n}^{N_R} T \times R_n^* + \sum_{n}^{N_R} T^* \times R_n, \end{aligned} \tag{4.16}$$

where N_R is the number of reference holes. The reference field $R_n(x, y)$ is approximately equal to the Fourier transform of a delta function. Because the reference apertures are displaced by (η, ζ) from the center of the image field in the image plane, $R_n(x, y)$ can be written as

$$R_n(x,y) = \mathcal{F}\{\delta(x - \eta, y - \zeta)\} = R_0^n \exp(2\pi i(x\eta + y\zeta)/\lambda z), \tag{4.17}$$

The goal of holographic reconstruction is to retrieve $t(X, Y)$ from Eq. 4.16, which can readily be

achieved by way of a simple Fourier transform, yielding

$$\mathcal{F}^{-1}\{I_{CCD}\} = t \otimes t^* + \sum_{n}^{N_R} R_n \otimes R_n^* + \sum_{n,m}^{n \neq m} R_n \otimes R_m^* + \sum_{n}^{N_R} T \otimes R_n^* + \sum_{n}^{N_R} T^* \otimes R_n, \qquad (4.18)$$

where $t = \mathcal{F}^{-1}\{T(x,y)\}$, $r_n = \mathcal{F}^{-1}\{R_n(x,y)\}$ and $\otimes$ indicates convolution. Constants and coordinate scaling factors have been neglected. The first two terms are the autocorrelation functions of the image and the reference fields at the image plane, and the last two terms are the cross-correlation of the object field with the reference field and their conjugates. The autocorrelation functions correspond to unwanted dc terms. Since the reference field at the image plane is a displaced delta function, the cross-correlation terms yield the object field information, $t(X,Y)$ and its complex conjugate $t^*(X,Y)$, displaced by (η,ζ) from the dc term [66].

Adequate separation between the reference holes and the objective window center is required in order to prevent the reconstructed object-field information, $t(X,Y)$, from overlapping with the dc terms. The maximum size of the object-field distribution at the image plane is determined by the size of the sample aperture. In Eq. 4.18 the first term, which is an autocorrelation function of the image field, has a maximum width twice the objective aperture size, and the cross-correlation terms have a maximum width equal to sample aperture. To prevent overlap between these two terms, the displacement has to be larger than 1.5 times the maximum object field size. The resolution of the spectro-holographic image recording technique depends on the reference holes diffraction; thus the reference hole diameter ultimately determines the smallest features that can be reconstructed. Given the diameter of the reference holes we should be able to reconstruct the image with a resolution of 50 nm.

The Fourier transform of the speckle intensity in Figure 4.9(b) after subtracting the dark noise is shown in Figure 4.10(a). The intense area in the center contains the autocorrelation terms in Eq. 4.18. The six circles offset from the center correspond to the cross-correlation of the reference holes with the sample. The vertical bright streaking comes from transmission through the gold mask and is also very dependent on how the missing pixels information has been replaced. The amplitude of the correction intensity in Figure 4.9(a) is chosen to minimize this effect.

Each pair of object images diagonally opposite to each other correspond to the same reference hole cross-correlation with the object field due to the symmetry of the Fourier-transform spectroholography imaging. Since we used three reference holes with different diameters, therefore there are three pairs of object image with different contrast and resolution. Therefore by averaging over the six object images we can acquire a higher signal to noise ratio (SNR) image of the sample

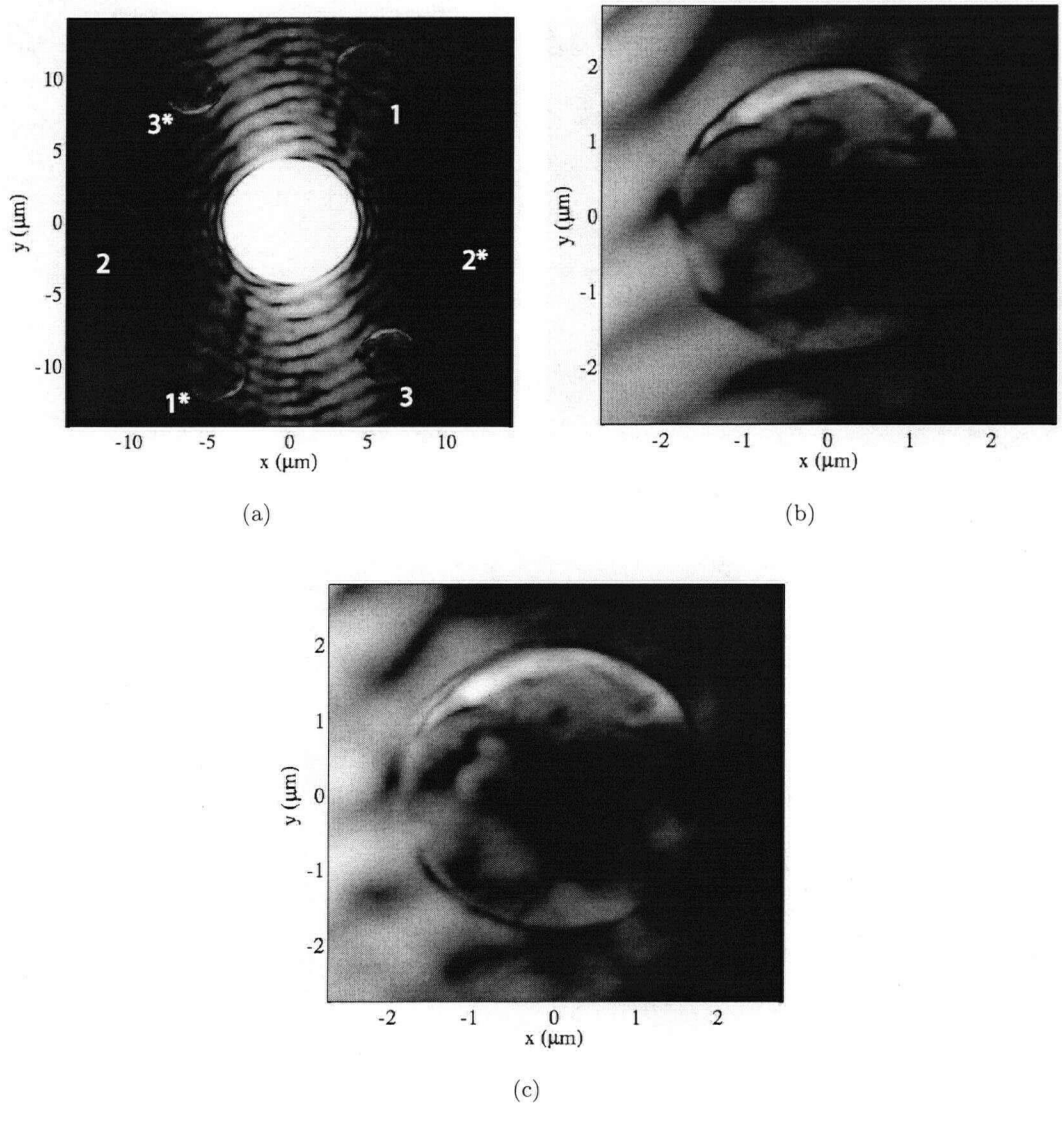

(a) (b)

(c)

Figure 4.10: (a) Reconstructed image from the hologram scattered intensity in the Figure 4.9(b). The six offset circles provides real space information on the object as described above; (b) magnified image of the second object in (a); (c) averaged object image over all object images in (a) showing 1.5× higher signal to noise ratio.

(See Figure 4.10(c)). Comparing the x-ray interference image with the SEM image we can see a high degree of consistency in terms of microstructures present in the RBC surface. In addition the x-ray image includes information about the elemental content of the RBC.

To investigate the sensitivity of our imaging technique to the presence of Fe in the form of hemoglobin molecules inside the cell we need to compare the reconstructed images captured near the Fe L_3-edge. Also in order to compare with experimental data we need an estimate of the amount of Fe inside the RBC. The average amount of hemoglobin inside a red blood cell is about 30 picograms [67], assuming the RBC has a spherical shape with a diameter of 5 μm. Given the molecular weight of the hemoglobin is 63,000 amu there is about 2.87×10^8 Hb/cell, estimating close packing of the Fe contents of the hemoglobin with average lattice spacing of 2.88 Å . This leads to 2.2 nm thick Fe layer inside the cell. The absorption from this amount of Fe using transmission data provided by Henke [56] is about 1.8 %. Including an edge-jump of 5 near the absorption edge taken from reference [68], we expect a 9 % change in the transmission at the absorption edge. As shown in the SEM image of the RBC5 sample, the aperture wasn't fully covered by the RBC, therefore we assume in the reconstructed image that the pixels with the maximum intensity correspond to 100 % transmission. We normalized all the pixel points inside the circular object field to the maximum intensity and plotted them as a function of energy averaged over two independent measurements near the Fe L_3-edge in Figure 4.11. The error bars come from the standard deviation of the two data sets. In this sparse data set we see about 8.5 % reduction in transmission near $E = 707$ eV.

Considering the experimental uncertainty this is in good agreement with the estimated value. The difference in the spectral width may come from the local molecular bonding of Fe atoms. In Figure 4.11(b) one can see how drastically the spectra differ by slight modification of the local molecular structure. We have no evidence of the local hemoglobin molecular structure after treating with fixative solution, thus it is reasonable to compare the spectrum with the heme-chloride spectrum presented in Figure 4.11(b).

Following a similar procedure near the C K-edge, the intensity distribution of the scattered x-rays on the detector is shown in Figure 4.12(a). The Fraunhofer diffraction rings due to the aperture are clearly larger than at $E = 707$ eV due to a 2.5 times longer wavelength. We can also see the speckle sizes along with the streaking from the reference holes magnified by approximately the same order as the wavelength. The individual speckle's size was about $\lambda L/S = 161$ μm with the given 13.5 μ m spacing on the detector, this leads to oversampling of 12 along each direction. The dynamic range of the interference pattern is defined by the ratio of the background noise to

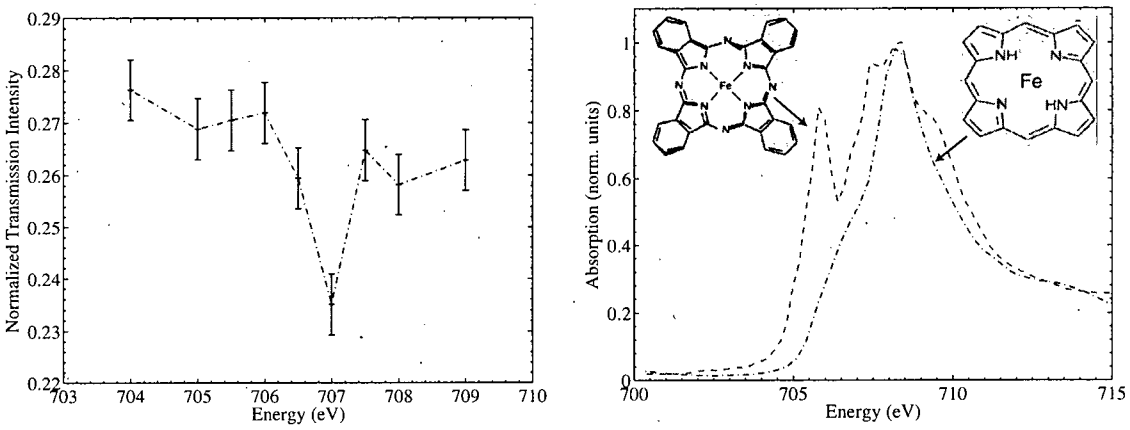

(a) (b)

Figure 4.11: (a) X-ray transmission measured near Fe L_3-edge using the reconstructed image; (b) fluorescence yield soft x-ray absorption from Fe-Phthalocyanin (red) and heme-chloride (blue) taken from reference [68]. The local Fe molecular structures are shown in the inset.

the maximum intensity, which is found to be 10^5. The transmission through 800 nm thick gold film at $E = 284$ eV is about 10^{-10} and through 100 nm Si_3N_4 is 45 %. One can notice a much smaller direct transmission through the gold mask and Si_3N_4 membrane compared to the former case with $E = 707$ eV. Therefore we should see less vertical streaking in the reconstructed image.

We mentioned above about the resolution determined by the reference hole diameter however in this case due to smaller momentum transfer the resolution is limited by $2\pi/q^{\parallel}_{max} = 70$ nm. We noticed a very large drop in the scattered intensity for measurements above $E = 285$ eV which was expected due to the large amount of carbon in the cell membrane structure and in the hemoglobin molecules inside the RBC. The Fourier transform reconstructed image from Figure 4.12(a) is presented in Figure 4.12(b). One can notice a weaker vertical streaking due to less transmission through the gold mask. For achieving higher SNR all the object images in Figure 4.12(b) are averaged. The averaged object image is shown in Figure 4.12(c).

We repeated the same type of normalization as we did for Fe L_3-edge measurements to quantify the sensitivity to carbon present in the cell. In practice this is a bit more challenging since there is also structure in the spectrum of the source due to carbon on the surface of beamline optical components. Therefore in addition we normalized the calculated intensity to the drain current of the horizontal focusing mirror (M_4 in Figure 4.6). The transmission data calculated

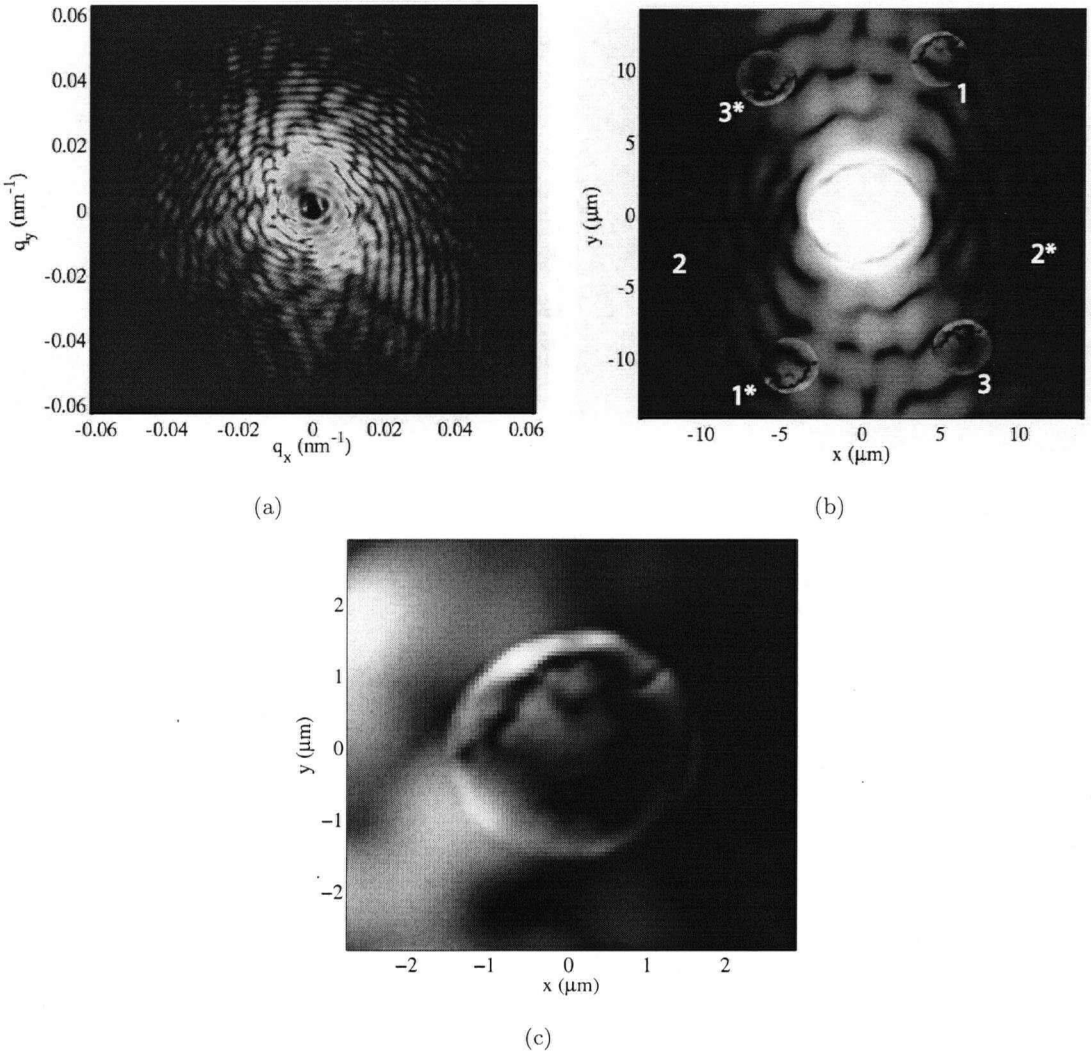

Figure 4.12: (a) Measured scattered intensity from sample RBC5 at E = 284 eV. Intensity is represented on a logarithmic color scale, with blue denoting the minimum intensity 10^2 and red denoting the maximum intensity of 10^6. The dynamic range of the interference pattern is 10^5; (b) reconstructed image from (a) using Fourier inversion; (c) averaged object image over all object images in (b).

near C K-edge is shown in Figure 4.13(a). Again the transmission has been calculated for two independent datatset and the error-bars come from the standard deviation of the two data-sets.

In order to get an estimate of the amount of carbon present inside the cell, let's assume a simple model in which there is only carbon from the hemoglobin inside the cell and it is uniformly distributed over a 5 μm diameter sphere. As described in the last chapter the hemoglobin is assembled from four polypeptide chains (two α and two β), where each contain a heme group in the hydrophobic pocket (See Figure 3.2(a)). The α and β chain each contain 141 and 146 amino acid residues respectively. The heme molecule is coordinated to the polypeptide chain through a histidine residue ($C_6H_9N_3O_2$), Figure 3.2(c). The empirical chemical formula of the most common human hemoglobin is $C_{2952}H_{4664}N_{812}O_{832}S_8Fe_4$ [69]. Using the same number of hemoglobins estimated above (2.87×10^8 Hb/cell) with close packing of carbon and average lattice spacing of 3.5 Å this lead to about 1.8 μm thick carbon layer inside the cell.

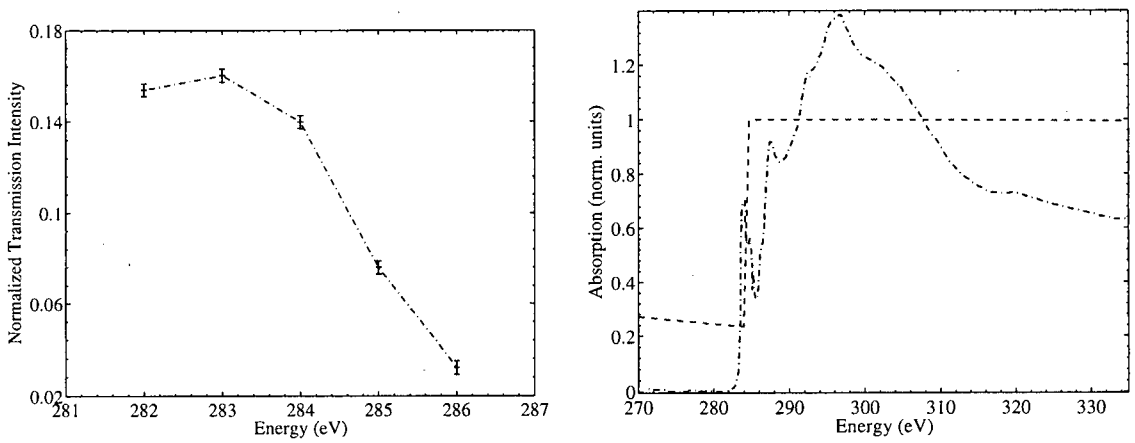

(a) (b)

Figure 4.13: (a) X-ray transmission measured near C K-edge using the reconstructed image; (b) total electron yield soft x-ray absorption near edge structure (XANES) measured near carbon K-edge from polyacetylene (PA) and x-ray white line absorption from 1.8 μm nm thick PA reprinted from [56, 70].

The x-ray absorption spectra for polyacetylene (PA) along with white line absorption through 1.8 μm PA is shown in Figure 4.13(b). The white line absorption shows very strong absorption above the edge for this amount of carbon hence we should expect very weak scattered intensity just above the C K-edge. Therefore all the scattered images captured were in the pre-edge region of the spectra. From this limited data-set we can find a lower bound for amount of carbon present

in the RBC using the reduction in the transmission intensity. In Figure 4.13(b) we notice about 80 % reduction in intensity and we estimated an edge-jump of 2 from the polyacetylene XAS data. The attenuation length of polyacetylene well above C K-edge ($E = 320$ eV) is about 330 nm, thus the lower limit on the thickness of carbon from our transmission measurement data is about $330 \times \ln(1/0.4) \simeq 300$ nm which lies well below the theoretical estimated value of 1.8 μm.

Chapter 5

Conclusion

In this work we presented some developments in lensless imaging using coherent x-ray scattering (CXS) from biological systems. As a common challenge in the field of microscopy the sample preparation is the most crucial step. In practice one wishes to have flexible sample which is suitable to as many techniques as possible. In the present work we showed successful microfabrication of sample-mask structures using focused ion beam milling which can be suitably used for CXS experiments on biological samples. In our experiment the mask is made from a 100 nm Si_3N_4 membrane that has been coated with a 600 - 800 nm gold film. We used commercially available Si_3N_4 membranes held by 3 mm diameter silicon frames that are designed for use in transmission electron microscopy. They are coated with gold by sputtering or electron beam evaporation. The sample to be imaged is mounted on the Si_3N_4 membrane in front of a 3 - 5 μm hole milled through the gold film on the opposite side. The ion milling is carried out with 30 keV Ga^+ ions using focused ion beam system at Simon Fraser University. A smaller 300 - 200 nm diameter tapered holes milled through both Au and Si_3N_4 layer at a 9 μm center-to-center distance away from the sample aperture were used as reference apertures for spectro-holographic lensless x-ray imaging [21].

For best x-ray imaging results, the focused ion beam milling should produce a circular aperture in the gold film with smooth vertical sidewalls, exposing the Si_3N_4 membrane at the bottom with no punctures, surface roughness or residual gold. We find that the gold surface roughens during ion milling due to sputter instability [38] producing cup-like surface features with a characteristic length up to few hundred nm. These features are imprinted on the membrane during the ion milling and can cause pinholes to form in the membrane before the gold is completely removed from bottom of the aperture. The surface roughness of the gold can be reduced by depositing the gold by sputtering rather than electron beam evaporation and by depositing the films on cold substrates ($-100°$C). Our apertures show good circularity and sidewall roughness of 20 nm.

Speckle simulation results on two different apertures with the characteristic (i) smooth side-

wall and rough bottom, (*ii*) smooth bottom and rough sidewall apertures are presented. The latter case showed a drastic change in the scattered intensity for the rough sidewall aperture forming speckles with sizes proportional to $\lambda L/S$ where L is sample-to-detector distance and S is the diameter of the aperture. The intensity distribution across an individual speckles is proportional to the sidewall roughness characteristic length. We decided to overcome the bottom roughness of the aperture by milling through the whole Si_3N_4 layer. This leads to a constraint on one lateral dimension of the sample under study. We found the red blood cells (RBCs) as an ideal biological system to practice our imaging technique. The RBCs were fixed using two fixative agents glutaraldehyde and OsO_4. A single RBC was mounted in front of the 3 μm diameter sample aperture on the Si_3N_4 side using the micromanipulation apparatus in Evan Evans lab at UBC hospital. The setup allowed to selectively mount echinocyte-spherocyte RBC in front of the objective aperture.

The CXS measurements were performed at the UE52/1-SGM beamline at BESSY II, Berlin. The x-ray images of the RBC were recorded near Fe L_3- and C K-edges. The reconstructed images showed good agreement with the SEM images of the RBC. We estimated a 9 % reduction in the transmitted intensity near Fe L_3-edge due to Fe in the hemoglobin molecules inside the RBC. We measured about 8.5 % reduction in transmission which agrees well with estimated 9 % effect within the experimental uncertainties. The object image showed resolution down to 52 nm which was constrained by the diameter of the smallest reference hole on the sample-mask structure. The reconstructed images near carbon K-edge showed much larger contrast. However in this case the resolution was constrained by the maximum in-plane momentum transfer rather than by the smallest reference hole diameter. The object image showed resolution down to 70 nm. In preparing the sample-mask structure we used three reference apertures with different diameters. This has an advantage of reconstructing images of the object with different contrast and resolution. As shown in the last chapter the spatial resolution of our imaging technique is determined by the size of the reference apertures. However reducing the reference aperture should be done while reducing x-ray transmission through the object or using smaller sample aperture size to control the relative sample and reference beam intensities. Therefore there is always a trade-off between contrast and resolution. Hence using reference holes with different diameter has the advantage of compensating for signal to noise ratio for images with low resolution and high contrast and images with high resolution and low contrast by averaging over all the sample images.

5.1 Future Experiments and Outlook

In our experiment we made use of a beamstop to achieve higher photon statistics for larger angle scattered photons and we replaced the beamstop with simulated data from the SEM image. This can introduce ambiguities to the reconstructed image. One can avoid this by recording the interference patterns first with a shorter exposure time without the beamstop and use this data to replace the missing information for the longer exposure time.

Another exciting possibility is an improvement in spatial resolution by application of iterative phase retrieval methods [5, 71–73] to the hologram. Our mask-based x-ray Fourier transform holography approach is fully compatibale with iterative phase retrieval, provided that the hologram is recorded with sufficient resolution. In a combined approach we record a high resolution x-ray hologram and the holographic image obtained by direct Fourier inversion is then used an the starting point for iterative refinement of the phase. In this way, ambiguities in the iterative process are restricted to the finest details of the image below the resolution of the holographic image. The ultimate resolution is then determined not by the reference pinhole size but by the maximum photon momentum transfer or, more specifically, by the wavelength. In parallel with phase reconstruction toward higher resolution imaging it would be ideal to have the detector mounted on the linear stage so it can be moved closer to the sample to record larger angle scattering which can be complemented the lower resolution images recorded at smaller angle scattering.

The present work was in part motivated by the expected availability of x-ray free electron lasers (XFEL) in the near future [74, 75]. Such sources will provide coherent high-brilliance x-ray pulses of femto-second duration. From the exposure time and coherent flux used for our images we can estimate that a single XFEL pulse will be sufficient to record an ultra-fast single shot image. This will open the door for taking ultra-fast movies of processes on the nanometer length scale. Our holographic approach is well matched to the spatial and temporal source properties of a XFEL and is a method of choice for single-shot ultra-fast imaging of the biological processes with such sources [76]. Another future application of the sample-mask structure is imaging the cells in water. This can lead to imaging live cells and avoiding fixative solutions to leave the actual cell contents untouched.

Bibliography

[1] H. N. Chapman, A. Barty, S. Marchesini, A. Noy, C. Cui, M. R. Howells, R. Rosen, H. He, J. C. H. Spence, U. Weierstall, T. Beetz, C. Jacobsen, and D. Shapiro. *J. Opt. Soc. Am. A* **23**, pp. 1179–1200, 2006.

[2] Z. H. Cai, B. Lai, W. B. Yun, I. McNulty, K. G. Huang, and T. P. Russel. *Phys. Rev. Lett.* **73**, pp. 82–85, 1994.

[3] D. Sayre and H. N. Chapman. *Acta Cryst. A* **51**, pp. 237–252, 1995.

[4] D. Sayre, H. N. Chapman, and J. Miao. *Acta Cryst. A* **54**, pp. 232–239, 1998.

[5] J. W. Miao, P. Charalambous, J. Kirz, and D. Sayre. *Nature* **400**, pp. 342–344, 1999.

[6] I. K. Robinson, I. A. Vartanyants, G. J. Williams, M. A. Pfeifer, and J. A. Pitney. *Phys. Rev. Lett.* **87**, p. 195505, 2001.

[7] G. J. Williams, M. A. Pfeifer, I. A. Vartanyants, and I. K. Robinson. *Phys. Rev. Lett.* **90**, p. 175501, 2003.

[8] S. Marchesini, H. He, H. N. Chapman, S. P. Hauriedge, A. Noy, M. R. Howells, and U. Weierstall. *Opt. Express* **11**, pp. 2344–2353, 2003.

[9] W. S. Haddad, I. McNulty, J. E. Trebes, E. H. Anderson, R. A. Levesque, and L. Yang. *Science* **266**, pp. 1213–1215, 1994.

[10] Y. Wang, C. Jacobsen, J. Maser, and A. Osanna. *J. Microsc.* **197**, pp. 80–93, 2003.

[11] D. Weib, G. Schneider, B. Niemann, P. Guttmann, D. Rudolph, and G. Schmahl. *Ultramicroscopy* **84**, pp. 185–197, 2000.

[12] C. A. Larabell and M. A. L. Gros. *Mol. Biol. Cell* **15**, pp. 957–962, 2004.

[13] R. Grimm, H. Singh, R. Rachel, D. Typke, W. Zilling, and W. Baumeister. *Biophys. J.* **74**, pp. 1031–1042, 1998.

[14] O. Madalia, I. Weber, A. Frangakis, D. Nicastro, G. Gerisch, and W. Baumeister. *Science* **298**, pp. 1209–1213, 2002.

[15] S. Wang, F. Duewer, F. Kamath, S. Kelly, C. Kelly, A. Lyon, K. Nill, P. Pombo, D. Scott, D. Trapp, and W. Yun. in *28th International Symposium for Testing and Failure Analysis*, p. 227, AMS International, (Phoenix, AZ), March 2002.

[16] D. Shapiro, P. Thibault, T. Beetz, V. Elser, M. R. Howells, C. Jacobsen, J. Kirz, E. Lima, H. M. A. M. Nieman, and D. Sayre. *Proc. Nat. Acad. Sci.* **102**(43), pp. 15343–15346, 2005.

[17] C. Jacobsen, R. Medenwaldt, and S. Williams., *X-ray Microscopy and Spectromicroscopy*, Springer, Berlin, 1998.

[18] I. Bernhardt and J. C. Ellory., *Red Cells Membrane Transport in Health and Disease*, Springer-Verlag, Berlin; Germany, 2003.

[19] E. Ponder., *Hemolysis and Related Phenomena*, Grune & Stratton, New York, 1948.

[20] G. H. W. Lim, M. Wortis, and R. Mukhopadhyay. *Proc. Natl. Acad. Sci.* **99**, pp. 16766–16769, 2002.

[21] S. Eisebitt, J. Lüning, W. F. Schlotter, M. Lörgen, O. Hellwig, W. Eberhardt, and J. Stöhr. *Nature* **432**, p. 885, 2004.

[22] R. F. Bunshah., *Handbook of Deposition Technologies for Films and Coatings*, Noyes Publication, Park Ridge; New York, 1994.

[23] J. L. Vossen and W. Kern., *Thin Film Processes II*, Academic Press Inc., San Diego, 1991.

[24] E. P. Graper. *J. Vac. Sci. Tech.* **8**, pp. 333–337, 1971.

[25] E. P. Kennedy, G. R. Schevermann, and H. R. J. Smith. *Res. Dev. Mag.* **22**, pp. 40–43, 1971.

[26] H. A. Beale and R. F. Bunshah. in *Proceeding 4th International Conference on Vacuum Metrology.*, p. 238, Iron and Steel Institute of Japan, (Tokyo, Japan), June 1973.

[27] L. I. Maissel and R. Galng., *Handbook of Thin film Technology*, McGraw Hill, New York, 1970.

[28] S. Schiller, U. Heisig, and S. Pranzer., *Electron Beam Technology*, John Wiley and Sons, New York, 1982.

[29] Y. Golan, L. Margulis, and I. Rubinstein. *Surf. Sci.* **264**, pp. 312–326, 1992.

[30] N. G. Semaltianos and E. G. Wilson. *Thin Solid Films* **366**, pp. 111–116, 2000.

[31] M. H. Dishner, M. M. Ivey, and S. G. J. C. Hemminger. *J. Vac. Sci. Technol. A* **16(6)**, pp. 3295–3300, 1998.

[32] K. Seshan., *Handbook of Thin-Film Deposition Processes and Techniques*, Materials Science and Processing Technology Series, William Andrew Publishing, New York, second ed., 2002.

[33] D. B. Fraser., *Handbook of Thin Film Technology*, McGraw Hill, New York, 1978.

[34] A. A. Tseng, I. A. Insua, J. S. Park, and C. D. Chen. *J. Vac. Sci. Technol. B* **22**, pp. 82–89, 2004.

[35] L. R. Harriott. *J. Vac. Sci. Technol A.* **8**, pp. 899–901, 1990.

[36] G. B. Assayag, C. Vieu, J. Gierak, P. Sudraud, and A. Corbin. *J. Vac. Sci. Technol. B* **11**, pp. 2420–2426, 1993.

[37] K. Edinger and T. Kraus. *J. Vac. Sci. Technol B.* **18**, pp. 3190–3193, 2000.

[38] M. Castro, R. Cuemo, L. Vazquez, and R. Gago. *Phys. Rev. Lett.* **94**, p. 16102, 2005.

[39] M. Bessis., *Living Blood Cells and their Ultrastructure*, Springer-Verlag, Berlin; Germany, 1973.

[40] D. L. Daleke and W. H. Huestis. *J. Cell. Biol.* **108**, pp. 1375–1378, 1989.

[41] H. F. Bunn and B. G. Forget., *Hemoglobin: Molecular, Genetic and Clinical Aspects*, WB Saunders, Philadelphia, 1986.

[42] R. S. Hillman and C. A. Finch., *Red Cell Manual*, F. A. Davis Company, Philadelphia, sixth ed., 1992.

[43] M. M. Wintrobe. *Folia Hemmat.* **51**, pp. 32–37, 1934.

[44] D. G. Dervichian, G. Fournet, and A. Guinier. *C. R. Acad. Sci.* **224**, pp. 1848–1852, 1947.

[45] J. T. Finch, M. F. Perutz, J. F. Bertles, and J. Döbler. *Proc. Nat. Acad. Sci.* **70**, pp. 718–722, 1973.

[46] D. C. Pease., *Histological Techniques for Electron Microscopy*, Academic Press Inc., London, 1964.

[47] B. F. Trump and R. Bulger. *Lab. Invest.* **15**, pp. 368–373, 1966.

[48] B. F. Trump and J. L. E. Ericsson. *Lab. Invest.* **14**, pp. 1245–1250, 1965.

[49] D. Hopwood. *Histochem. J.* **1**(4), pp. 323–360, 1969.

[50] D. Hopwood. *Histochem. J.* **4**(4), pp. 267–303, 1972.

[51] R. B. Litman and R. J. Barrnet. *J. Ultrastruct. Res.* **38**, pp. 63–86, 1972.

[52] H. Schiechl. *Acta. Histochem. Suppl.* **10**, pp. 165–172, 1971.

[53] J. R. Hollahan and A. T. Bell., *Techniques and Applications of Plasma Chemistry*, John Wiley & Sons, New York, 1974.

[54] E. Evans, K. Ritchie, and R. Merkel. *Biophys. J.* **68**, pp. 2580–2588, 1995.

[55] D. Attwood., *Soft X-rays and Extreme Ultraviolet Radiations: Principles and Applications*, Cambridge University Press, Cambridge, 2000.

[56] B. Henke, E. Gullikson, and J. Davis. *Atomic Data and Nuclear Data Tables* **54**, pp. 181–342, 1993.

[57] M. Born and E. Wolf., *Principles of Optics: Electromagnetic Theory of Propagation, Interference and Diffraction of Light*, Cambridge University Press, Cambridge, seventh ed., 1999.

[58] F. van der Veen and F. Pfeiffer. *J. Phys.: Condens. Matter* **16**, pp. 5003–5030, 2004.

[59] S. Eisebitt, M. Lörgen, W. Eberhardt, J. Lüning, and J. Stöhr. *Appl. Phys. A.* **80**, pp. 921–927, 2005.

[60] J. Miao, T. Ishikawa, E. H. Anderson, and K. O. Hodgson. *Phys. Rev. B* **67**, p. 174104, 2003.

[61] A. Rahmim, S. Tixier, T. Tiedje, S. Eisebitt, M. Lörgen, R. Scherer, W. Eberhardt, J. Lüning, and A. Schöll. *Phys. Rev. B* **65**, p. 235421, 2002.

[62] F. Senf, F. Eggenstein, U. Flechsig, R. Follath, S. Hartlaub, H. Lammert, T. Noll, J. S. Schmidt, G. Reichardt, O. Schwarzkopf, M. Weiss, T. Zeschke, and W. Gudat. *Nucl. Instr. and Meth. A* **467-468**, pp. 474–478, 2001.

[63] F. Senf, H. Lammert, , R. Follath, . Zeschke, W. Gudat, K. Feichtinger, P. Fischer, W. Hubner, and R. Strobel. *J. Synchrotron Rad.* **5**, pp. 584–586, 1998.

[64] G. Grabis, A. Nefedov, and H. Zabel. *Rev. Sci. Instrum.* **74**(9), pp. 4048–4051, 2003.

[65] J. Goodman., *Introduction to Fourier Optics*, McGraw Hill, New York, second ed., 1996.

[66] G. W. Stroke., *An Introduction to Coherent Optics and Holography*, Academic, New York, 1969.

[67] B. J. Bain., *Blood Cells: A Practical Guide*, Blackwell, Malden, MA, 2006.

[68] M. Freiwald, S. Cramm, W. Eberhardt, and S. Eisebitt. *J. Electron Spectros. and Relat. Phenom.* **137-140**, pp. 413–416, 2004.

[69] F. A. Cotton, G. Willkinson, C. A. Murillo, and M. Bochmann., *Advanced Inorganic Chemistry*, John Wiley and Sons, New York, sixth ed., 1999.

[70] M. G. Kim, H. J. Lee, B. H. Kim, J. S. Kim, and Y. W. Park. *Physica Scripta* **T115**, pp. 393–395, 2005.

[71] R. W. Gerchberg and W. O. Saxton. *Optik* **35**, pp. 237–246, 1972.

[72] J. R. Fienup. *Appl. Opt.* **21**, pp. 2758–2769, 1982.

[73] J. R. Fienup. *J. Opt. Soc. Am.* **4**, pp. 118–124, 1987.

[74] A. Cho. *Science* **296**, pp. 1008–1010, 2002.

[75] P. Emma, K. Bane, M. Cornacchia, Z. Huang, H. Schlarb, G. Stupakov, and D. Walz. *Phys. Rev. Lett.* **92**, p. 074801, 2004.

[76] J. Kirz. *Nature Phys.* **2**, pp. 799–800, 2006.

Part I

Appendices

Appendix A

Speckle Simulation Matlab Code

```
%2D SPECKLE SIMULATION AUGUST 2006

tic;

%IMPORT IMAGE

load AFM_Data.txt %loading formatted AFM data
smp=double(sample);
disp('Image Loaded');

%DEFINE GEOMETRY OF SIMULATION

R=3000e6; %obj and detector center to center distance in nm
R_p=50e6; %center to center distance between the pinhole
%and the object in nm


smpSizeArray=size(smp);
smp_Size=smpSizeArray(1,1);
img_size_x=160; %number of pixel on CCD horiz
img_size_y=160; %number of pixel on CCD vert
half_smp_size=round(smp_Size/2);
half_img_x=round(img_size_x/2); %mid point on the image
half_img_y=round(img_size_y/2);

smp_pix_size=6.5e3/smp_Size*20; %spacing between points on the
```

```
%image in nm
x=linspace(-half_smp_size,half_smp_size,smp_Size)*smp_pix_size;
%x coord along the Sample in nm
y=linspace(-half_smp_size,half_smp_size,smp_Size)*smp_pix_size;
%y coord along the Sample in nm
[X,Y]=meshgrid(x,y); %matrix containg x and y coord of the object

img_pix_size=50e3/2/3; %spacing between pixels on CCD in nm

%PHOTON CHARACTERISTICS

E=700; %photon energy in eV
lambda=1248/E; %photon wavelength in nm
Ko=2*pi/lambda; %photon K vector norm in nm-1
a=5e3; %radius of the pinhole in nm

Lobj = smp_Size*smp_pix_size; % size of the object in nm


xx_img = linspace(-half_img_x,half_img_x,img_size_x)*img_pix_size;
%X coord along image in nm
yy_img = linspace(-half_img_y,half_img_y,img_size_y)*img_pix_size;
%Y coord along image in nm
[x_img,y_img]=meshgrid(xx_img,yy_img); %matrix containing X and Y
%coord of the image
dX = Lobj/(smp_Size-1); %X coord Pixel Spacing on Detector
dY = dX; %Y coord Pixel Spacing on Detector
ci = sqrt(-1);


detect_field = zeros(img_size_x,img_size_y);
%Initializing Detector E-Field
r=zeros(smp_Size,smp_Size);
Int_Pts=ones(smp_Size,smp_Size); %Initializing Pinhole
```

```
%Radiation Matrix
pts_calced = 0;

prefactor = ci/lambda*dX*dY; %Prefactor

%CALCULATING RADIATION FROM A PINHOLE WITH RADIUS 'a'
%OVER THE SAMPLE AT A DISTANCE R_P USING ANALYTICAL SOLUTION


for i=1:smp_Size,
   for j=1:smp_Size,
      Int_Pts(i,j)=(2*besselj(1,Ko*a*sqrt(X(i,j)^2+Y(i,j)^2)/R_p)/...
      (Ko*a*sqrt(X(i,j)^2+Y(i,j)^2)/R_p))^2;
   end
end


%SCATTERING SIMULATION

for i=1:smp_Size,
   for j=1:smp_Size,
      if smp(i,j)>0, % only calculate when sample is non-zero
         pts_calced = pts_calced+1;
         r = sqrt( (X(i,j)-x_img)^2 + (Y(i,j)-y_img)^2 + R^2 );
         %Matrix containing distances from
         %all smp pixels to img pixels
         detect_field= detect_field+Int_Pts(i,j)*smp(i,j)*...
         prefactor*exp(ci*Ko*r)./r;
      end
   end
end

pts_calced
```

```
%PLOTTING THE SIMULATION RESULT

figure(1)
clf
pcolor(X,Y,smp)
shading flat
xlabel('X (nm)')
ylabel('Y (nm)')
colorbar

figure(2)
clf
pcolor(X*Ko/R_p,Y*Ko/R_p,log(Int_Pts))
shading flat
xlabel('qx (nm-1)')
ylabel('qy (nm-1)')
colorbar

figure(3)
clf
pcolor(x_img*Ko/R,y_img*Ko/R,log(abs(detect_field).^2))
xlabel('qx (nm-1)')
ylabel('qy (nm-1)')
colorbar
shading flat

toc;
```